

Ordered magnetism in the intrinsically decorated $j_{\text{eff}} = \frac{1}{2} \alpha\text{-CoV}_3\text{O}_8$

P. M. Sarte,^{1,2} A. M. Arévalo-López,^{1,2,3} M. Songvilay,^{2,4} D. Le,⁵ T. Guidi,⁵ V. García-Sakai,⁵ S. Mukhopadhyay,⁵ S. C. Capelli,⁵ W. D. Ratcliff,⁶ K. H. Hong,^{1,2} G. M. McNally,^{1,2,7} E. Pachoud,^{1,2} J. P. Attfield,^{1,2} and C. Stock^{2,4}

¹*School of Chemistry, University of Edinburgh, Edinburgh EH9 3FJ, United Kingdom*

²*Centre for Science at Extreme Conditions, University of Edinburgh, Edinburgh EH9 3FD, United Kingdom*

³*Université Lille 1 Sciences et Technologies, UMR 8181 CNRS,*

Unité de Catalyse et Chimie du Solide 'UCCS', 59655 Villeneuve d'ASCQ, France

⁴*School of Physics and Astronomy, University of Edinburgh, Edinburgh EH9 3FD, United Kingdom*

⁵*ISIS Facility, Rutherford Appleton Laboratory, Chilton, Didcot OX11 0QX, United Kingdom*

⁶*NIST Center for Neutron Research, National Institute of Standards and Technology, Gaithersburg, Maryland 20899, USA*

⁷*Max-Planck-Institut für Festkörperforschung, D-70569 Stuttgart, Germany*

(Dated: December 10, 2018)

The antiferromagnetic mixed valence ternary oxide $\alpha\text{-CoV}_3\text{O}_8$ displays disorder on the Co^{2+} site that is inherent to the *Ibam* space group resulting in a local selection rule requiring one Co^{2+} and one V^{4+} reside next to each other, thus giving rise to an intrinsically disordered magnet without the need for any external influences such as chemical dopants or porous media. The zero field structural and dynamic properties of $\alpha\text{-CoV}_3\text{O}_8$ have been investigated using a combination of neutron and x-ray diffraction, DC susceptibility, and neutron spectroscopy. The low temperature magnetic and structural properties are consistent with a random macroscopic distribution of Co^{2+} over the $16k$ metal sites. However, by applying the sum rules of neutron scattering we observe the collective magnetic excitations are parameterized with an ordered Co^{2+} arrangement and critical scattering consistent with a three dimensional Ising universality class. The low energy spectrum is well-described by Co^{2+} cations coupled *via* a three dimensional network composed of competing ferromagnetic and stronger antiferromagnetic superexchange within the *ab* plane and along *c*, respectively. While the extrapolated Weiss temperature is near zero, the 3D dimensionality results in long range antiferromagnetic order at $T_N \sim 19$ K. A crystal field analysis finds two bands of excitations separated in energy at $\hbar\omega \sim 5$ meV and 25 meV, consistent with a $j_{\text{eff}} = \frac{1}{2}$ ground state with little mixing between spin-orbit split Kramers doublets. A comparison of our results to the random 3D Ising magnets and other compounds where spin-orbit coupling is present indicate that the presence of an orbital degree of freedom, in combination with strong crystal field effects and well-separated j_{eff} manifolds may play a key role in making the dynamics largely insensitive to disorder.

I. INTRODUCTION

Introducing disorder into condensed matter systems often suppresses common mean-field phases and transitions in favor of states that exhibit unusual critical properties¹⁻¹². Examples of such exotic behavior in insulating systems include the study of quenched disorder through doping in both model magnets^{13,14} and liquid crystal systems¹⁵⁻¹⁷. While the presence of strong disorder disrupts translational symmetry, often resulting in a glassy phase¹⁸ with long range order destroyed for all length scales, the presence of weak disorder can give rise to phases displaying distinct responses for differing length scales. For example, in model random field systems near a phase transition, critical thermal fluctuations dominate until the length scale of the order parameter becomes large enough where static terms originating from the induced disorder dominate^{19,20}. Examples of new disordered-induced phases include the concept of "Bragg glass"²¹⁻²⁵ that were first postulated in the context of flux lattices in superconductors²⁶⁻²⁸ where Bragg peaks exist, however other properties reflect a glass type response. A further example of unusual phases in the presence of disorder is the Griffiths phase²⁹⁻³¹ that was first suggested in the context of Ising ferromagnets, where an ordered local region co-exists within a globally disordered phase. So far, the search for new disordered-induced phases have been limited to introducing disorder by doping in the case of solid state materials, or porous media for liquid crystals^{16,32-34} and quantum fluids³⁵⁻³⁹.

One example of theoretical efforts to understand the

effects of quenched disorder on the order parameter near a phase transition is random field theory which relates disorder to the lowering of the dimensionality of the underlying universality class^{40,41}. Model random magnets^{13,14,42,43} have played a significant role in the development and validation of such theories with an important example being the dilute Ising antiferromagnets such as $\text{Fe}_x\text{Zn}_{1-x}\text{F}_2$ ^{6,44-46} (Fe^{2+} , $L = 2$ and $S = 2$) and $\text{Mn}_x\text{Zn}_{1-x}\text{F}_2$ ^{47,48} (Mn^{2+} , $L = 0$ and $S = \frac{5}{2}$). In these magnets, the random occupancy introduced through doping combined with a magnetic field results in a tunable random field. While these systems show a competition between static and thermal fluctuations driving magnetic order, the dynamics are largely unaltered by the introduction of weak disorder^{49,50} and therefore the magnets with weak quenched disorder have collective dynamics very similar to the parent compounds. Despite significant interest in the community⁵¹, the amount of systems that have been shown to host such exotic phases as described above have been limited, in particular, there are few examples of definitive Bragg glass and Griffiths phases. In this paper, we discuss a system where disorder is not introduced through doping, but rather is inherent to the crystallographic symmetry and therefore is a situation where magnetic disorder is present despite the presence of structural order.

In contrast to the disordered systems described above, where the disorder is a consequence of an addition external to the original system (*e.g.* doping^{6,44-48}, porous media^{32,37,38}, *etc.*), and thus can be finely tuned⁵⁴, the disorder in $\alpha\text{-CoV}_3\text{O}_8$ is simply inherent to its *Ibam* crystal structure. As illustrated in Figs. 1(a) and (b), the pro-

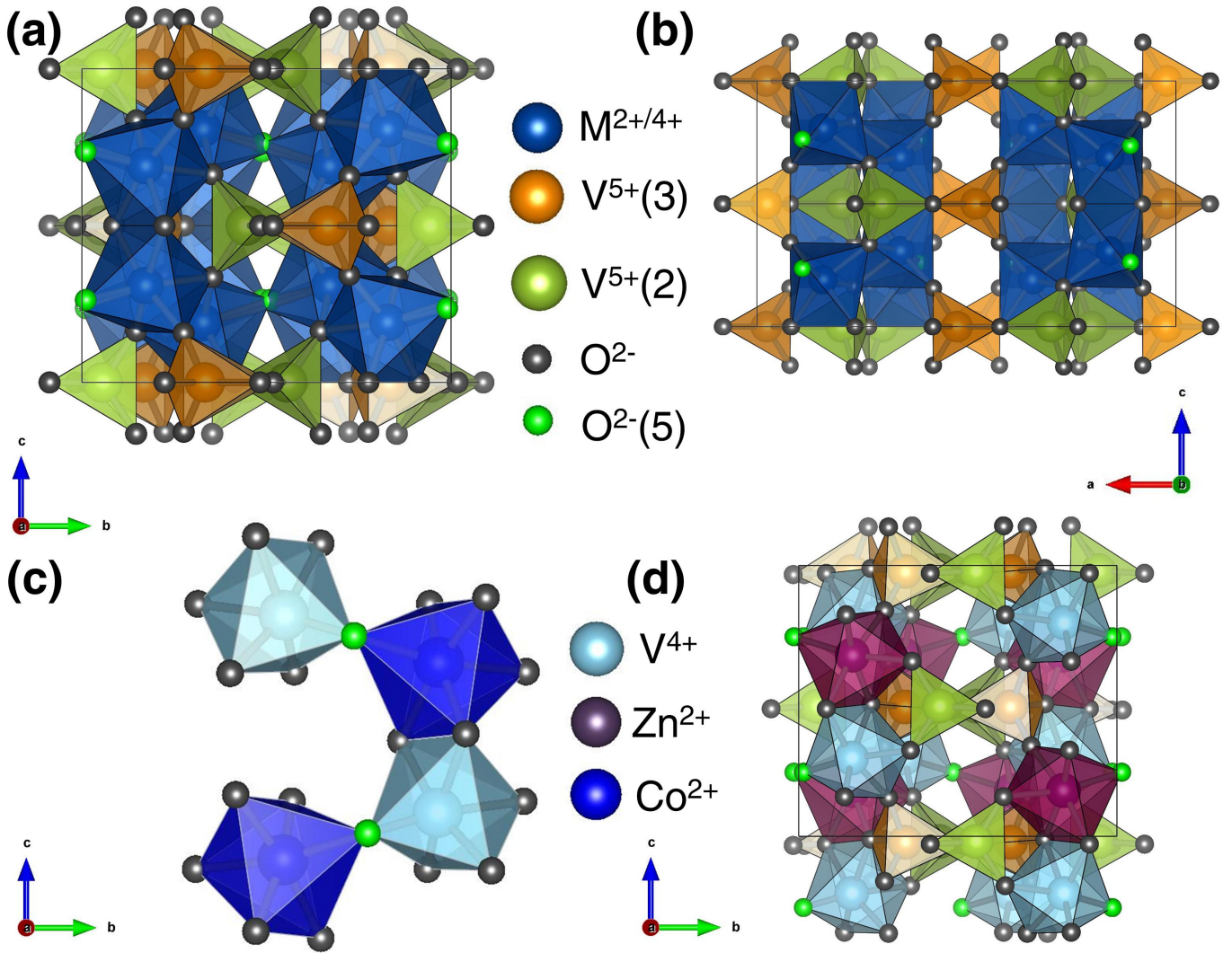


FIG. 1. Proposed⁵² crystal structure of α - CoV_3O_8 (*Ibam*, #72) along the (a) bc and (b) ac planes, consisting of zigzag chains of edge-sharing MO_6 ($M = \text{Co}^{2+}$, V^{4+}) octahedra running parallel to c that are interspaced with non-magnetic V^{5+} in tetrahedral ($\text{V}^{5+}(2)$) and trigonal bipyramidal ($\text{V}^{5+}(3)$) coordination. (c) Local constraint of the *Ibam* structure. Metal sites opposite of the bridging O(5) must be occupied by one Co^{2+} and one V^{4+} , with the O(5) situated closer to the V^{4+} site. (d) Crystal structure of α - ZnV_3O_8 (*Iba2*, #45). In contrast to *Ibam*, the *Iba2* structure consists of an ordered alternating distribution of Zn^{2+} and V^{4+} along the zigzag chains⁵³.

posed⁵² crystal structure of α - CoV_3O_8 consists of zigzag chains of edge-sharing MO_6 octahedra ($M = \text{Co}^{2+}$ and V^{4+}) running along c . With the exception of a single crystallographic constraint corresponding to a local selection rule requiring that one Co^{2+} and one V^{4+} reside on opposite sides of the O(5) bridging oxygen (Fig. 1(c)), the *Ibam* structure of α - CoV_3O_8 consists of a random distribution of metal cations along the zigzag chains. A combination of the proposed random metal cation distribution with both evidence⁵² for dominant antiferromagnetic exchange coupling from DC susceptibility and Ising anisotropy due to local axial octahedral distortions and spin-orbit coupling, suggests that α - CoV_3O_8 may represent a potential alternative route for the investigation of disordered-induced physics. Indeed the study of disorder on electronic structures has found that by introducing correlations, localization⁵⁵ can be suppressed.^{56,57}

In this paper, we characterize both the crystal-magnetic structure and fluctuations of α - CoV_3O_8 . This paper consists of five sections discussing our results including this introduction and a subsequent section on

experimental details. We first present the characterization of the static nuclear-magnetic structure. High resolution single crystal x-ray and neutron diffraction data confirmed both the disordered *Ibam* crystal structure and the presence of local octahedral distortions. A combination of single crystal magnetic neutron diffraction and single crystal DC susceptibility identified the presence of ferromagnetic correlations between Co^{2+} cations within the ab plane, in addition to a dominant antiferromagnetic coupling along c . Low energy critical scattering is consistent with 3D Ising behavior attributable to the $j_{\text{eff}} = \frac{1}{2}$ Co^{2+} ions. However, in contrast to the intrinsically disordered *Ibam* crystal structure, by applying the first moment sum rule of neutron scattering, we find the excitations are well described by an ordered Co^{2+} arrangement. We conclude the paper with a section discussing our results in the context of models for disordered magnets and discuss the role of spin-orbit coupling through a comparison of model magnets in a random field.

II. EXPERIMENTAL DETAILS

Sample Preparation: Single crystals of α -CoV₃O₈ were grown using a modified “self-flux” heating routine for α -CoV₂O₆⁵⁸. Precursor polycrystalline samples of α -CoV₂O₆ were first synthesized by a standard solid-state reaction consisting of heating a stoichiometric mixture of Co(CH₃CO₂)₂ · 4 H₂O (Sigma-Aldrich, 98%) and V₂O₅ (Alfa Aesar, 99.6%) in air for 12 h at 650°C, then for 48 h at 725°C, followed by quenching in liquid nitrogen^{59,60}. A mixture of the α -CoV₂O₆ polycrystalline precursor and V₂O₅ in a 3:2 ratio in the presence of approximately 0.01% (*w/w*) of B₂O₃ (Alfa Aesar, 98.5%) was heated in a vacuum sealed quartz tube at 780°C for 24 h and subsequently cooled to 700°C at a rate of 1°C hr⁻¹. After 24 h of heating at 700°C, the sample was cooled to 600°C at a rate of 1°C hr⁻¹ and subsequently quenched to room temperature.

Polycrystalline samples of α -CoV₃O₈ and α -ZnV₃O₈ were synthesized by a standard solid-state reaction consisting of heating a stoichiometric mixture of CoO (Alfa Aesar, 95%) or ZnO (Alfa Aesar, 99.99%), VO₂ (Alfa Aesar, 99%) and V₂O₅ for 96 h at 650°C under static vacuum in a sealed quartz tube with intermittent grindings until laboratory powder x-ray diffraction confirmed no discernable impurities^{53,61}. All stoichiometric mixtures of polycrystalline precursors were first mixed thoroughly together and finely ground to homogeneity with acetone using an agate mortar and pestle. The mixtures were pressed into \sim 2 g pellets using a uniaxial press and subsequently placed in alumina crucibles or directly in quartz ampoules for reactions performed in air and in vacuum, respectively. Unless otherwise stated, all heating routines involved a ramping rate of 5°C min⁻¹ and samples were furnace cooled back to room temperature.

Laboratory X-ray Diffraction: Single crystal x-ray diffraction was performed at 120 K on a 0.011 mg single crystal of α -CoV₃O₈ with dimensions of 0.40 × 0.11 × 0.09 mm³ using monochromated Mo K _{α} radiation on an Oxford Diffraction SuperNova dual wavelength diffractometer equipped with an Atlas CCD detector and an Oxford Cryostream-Plus low-temperature device. Data collection, integration, scaling, multiscan absorption corrections and indexing were performed using the CrysAlisPro v1.171.37.35e software package⁶². The structure solution was performed using a direct approach method with the SHELXS-97 program in Olex2⁶³.

Room temperature powder diffraction patterns of α -CoV₂O₆, α -CoV₃O₈ and α -ZnV₃O₈ were collected over $2\theta = [5, 70]^\circ$ in 0.0365° steps on a Bruker D2 Phaser laboratory x-ray diffractometer using monochromated Cu K _{α} radiation.

All structural refinements for single crystal and polycrystalline measurements were performed using the JANA2006⁶⁴ and GSAS⁶⁵ Rietveld refinement program packages, respectively, and are summarized in Appendix A. For the single-crystal refinement, the solved structure was refined by a full-matrix least squares against F^2 using only data $I > 3\sigma(I)$.

DC Magnetic Susceptibility: A 7.7 mg single crystal of α -CoV₃O₈ with dimensions of 2 × 1 × 1 mm³ was aligned along the three principal axes. All crystal alignments were performed with polychromatic Laue backscattering diffraction employing adapted photostimulable plates using the Fujifilm FCR Capsula XL II system⁶⁶. The temperature dependence of ZFC magnetization for all three principal axes was measured on a Quantum Design MPMS in an external DC field $\mu_0 H_{\text{ext}} = 0.5$ T applied parallel to the particular axis of interest. Measurements were performed in 2 K steps spaced linearly from 2 K to 300 K.

Neutron Single Crystal Diffraction: Neutron single crystal diffraction experiments were performed on the SXD^{67,68} time-of-flight instrument at the ISIS spallation source. The SXD diffractometer employs the time-of-flight Laue technique. The combination of a polychromatic incident beam falling on a stationary sample surrounded by 11 ZnS scintillator PSDs covering $\Omega \sim 2\pi$ sr enables quick access to a large amount of reciprocal space with minimal sample movement during data collection. A 0.4312 g single crystal of α -CoV₃O₈ with dimensions of 13.2 × 4.1 × 2.1 mm³ as illustrated in Fig. 2(d) was mounted on the end of a 6 mm aluminum pin with aluminum tape, vertically suspended from a liquid helium 50 mm bore Orange cryostat providing ω -motion in an accessible temperature range of 1.5 to 300 K. Diffraction data was collected at both 5 K and 50 K for three different single crystal frames with an accumulated charge of 1300 $\mu\text{A}\cdot\text{h}$ (\sim 8 h). After each temperature change, the sample was allowed to thermalize for 15 minutes. Reflection intensities were extracted, reduced and integrated to structure factors using standard SXD procedures, as implemented in SXD2001⁶⁷⁻⁶⁹.

Inelastic Neutron Time-of-Flight Scattering Spectroscopy: All inelastic neutron scattering experiments were performed on the direct geometry MARI^{70,71} and indirect geometry IRIS⁷² time-of-flight spectrometers located at ISIS. Neutron spectroscopic measurements were performed on powders as preliminary measurements found the signal from single crystals to be weak. High-energy measurements (> 2 meV) on 32.6 g of α -CoV₃O₈ and 31.9 g of α -ZnV₃O₈ were performed on the direct geometry MARI spectrometer. The t_0 chopper was operated at 50 Hz in parallel with a Gd chopper spun at 350, 300 and 250 Hz with incident energies $E_i = 150, 60$ and 15 meV, respectively, providing an elastic resolution of 5.87, 1.82 and 0.321 meV, respectively. A thick disk chopper spun at $f = 50$ Hz reduced the background from high-energy neutrons. A top loading Displex CCR provided an accessible temperature range of 5 to 600 K.

For lower energies, measurements on 15.1 g of α -CoV₃O₈ were performed on the indirect geometry IRIS spectrometer. As an indirect geometry spectrometer, the final energy E_f was fixed at 1.84 meV by cooled PG002 analyzer crystals in near backscattering geometry. The graphite analyzers were cooled to reduce thermal diffuse scattering⁷³, providing an elastic resolution of 17.5 μeV . A top loading Displex CCR provided an accessible temperature range of 5 to 580 K.

Neutron Powder Diffraction: Neutron diffraction measurements on 1.8 g of polycrystalline α - CoV_3O_8 were performed on the BT-4 thermal triple axis spectrometer⁷⁴ at the NIST Center for Neutron Research (NCNR). Incident and scattering neutron energies were set to 14.7 meV ($\lambda=2.3592$ Å), selected by vertically focussing PG002 monochromator and analyzer crystals with PG filters located before and after the sample to reduce higher-order neutron contamination. The Söller horizontal collimator configuration downstream order was 60'-monochromator-80'-sample-80'-analyzer-60'-detector. A top loading liquid helium 50 mm bore Orange cryostat provided an accessible temperature range of 1.5 to 300 K. θ - 2θ measurements were collected at both 3 K and 300 K over $2\theta = [15, 90]^\circ$ in 0.2° steps ($|\mathbf{Q}| = [0.695, 3.766]$ Å⁻¹ in 0.009 Å⁻¹ steps). Magnetic order parameter measurements were performed at $2\theta = 41.6^\circ$ ($|\mathbf{Q}| = 1.89$ Å⁻¹) over $T=[3, 32]$ K in 0.1 K steps.

III. RESULTS & ANALYSIS

A. Crystal Structure

As illustrated in Fig. 2(a) and summarized in Tabs. V-VI in Appendix A, single crystal x-ray diffraction at 120 K confirmed an orthorhombic unit cell ($a = 14.29344(4)$ Å, $b = 9.8740(3)$ Å, $c = 8.34000(3)$ Å) with a volume of $1185.60(6)$ Å³, corresponding to $Z = 8$. Systematic extinctions provided $Ibam$ (#72, Fig. 1(a,b)) and $Iba2$ (#45, Fig. 1(d)) as possible space groups, with statistical analysis of the intensity data favoring the centrosymmetric $Ibam$. In a procedure analogous to previous studies on hydrothermally grown single crystals, the structure was solved using a direct method⁵². The corresponding unit cell was found to consist of three metal sites with octahedral ($16k$), tetrahedral ($8j$) and trigonal bipyramidal ($8j$) coordination, with Co^{2+} and V^{4+} with half occupancies independently distributed over the $16k$ site and V^{5+} with full occupancies in the latter two $8j$ sites. Structural refinements utilizing 910 out of a total of 985 measured reflections confirmed two important conclusions from previous studies^{52,61}. Firstly, Co^{2+} and V^{4+} are both randomly and equally distributed over the $16k$ site with refined occupancies of $0.506(6)$ and $0.494(4)$, respectively. Secondly, the large refined anisotropic displacements resulting from placing the O(5) oxygen in the $8f$ position with full occupancy support the local selection rule consisting of Co^{2+} and V^{4+} occupying respective positions on opposite sides of the O(5) bridging oxygen ligand, as illustrated in Fig. 1(c).

B. DC Magnetic Susceptibility

As summarized by Tab. I and Fig. 2, DC susceptibility measurements along all three principal axes indicates that α - CoV_3O_8 behaves as a Curie-Weiss paramagnet at high temperatures and undergoes an antiferromagnetic transition at $19.5(5)$ K, corresponding to a T_N much greater than previously reported T_N of 8.2 K for crystals

TABLE I. Curie-Weiss parameters^a for α - CoV_3O_8 in an external DC field $\mu_0 H_{\text{ext}} = 0.5$ T applied parallel to the three principal axes. Numbers in parentheses indicate statistical errors.

Crystallographic Axis	C (emu K/mol)	p_{eff} (μ_B)	θ_{CW} (K)
a	3.525(9)	5.310(7)	9.5(7)
b	3.31(2)	5.15(2)	2(1)
c	3.354(2)	5.180(2)	-21.3(2)
Average	3.396(7)	5.213(7)	-3.2(4)

^a Calculated over a range of $150 \leq T \leq 300$ K

grown hydrothermally⁵². A fit of the high temperature data (Fig. 2b) to the Curie-Weiss law yielded Curie-Weiss temperatures θ_{CW} of 9.5(7), 2(1), $-21.3(2)$ K for $\mu_0 H_{\text{ext}}$ applied along a , b and c , respectively. The small θ_{CW} with an average $\theta_{\text{CW}} = -3.2(4)$ K is suggestive of either weak exchange interactions or the presence of multiple and nearly canceling ferro/antiferromagnetic interactions resulting in the experimentally observed small average. The differences in the constants measured along different directions is also indicative of an anisotropy in the system likely originating from the distortion of the local octahedra^{60,75}.

As illustrated in Fig. 2(b), the magnetization does not approach zero in the low temperature limit after the antiferromagnetic transition. Instead, its value for all three principal axes plateaus at 2 K which indicates the possibility for the presence of paramagnetism at lower temperatures, although no measurements were conducted below 2 K. In contrast to the d^7 Co^{2+} moments that can couple *via* e_g orbitals, coupling between the d^1 V^{4+} moments are exclusively *via* t_{2g} orbitals which is predicted to be much weaker⁷⁶⁻⁷⁸ and thus more likely to exhibit paramagnetic behavior. In fact, V^{4+} paramagnetism is supported by the observation that the saturated moment in the low temperature limit corresponds to $0.150(2)$ μ_B , a value consistent with a strongly reduced V^{4+} effective paramagnetic moment predicted to occur in the presence of strong spin-orbit coupling and octahedral distortions as has been previously observed experimentally in $\text{Na}_2\text{V}_3\text{O}_7$ ^{79,80}. Finally, the average effective paramagnetic moment of $5.213(7)$ μ_B is smaller than the predicted moment of 5.6 μ_B , for Co^{2+} in an octahedral environment as studied in CoO ⁸¹ and assuming a 1:1 ratio of high spin Co^{2+} and V^{4+} , confirming that both spin-orbit and distortion effects play a significant role^{59,82} in the magnetism of α - CoV_3O_8 , a topic that will be later addressed with inelastic neutron scattering.

C. Magnetic Structure

As shown in Fig. 2(c) and summarized in Tabs. VII-VIII in Appendix A, single crystal neutron diffraction confirmed both an absence of any structural distortion away from the $Ibam$ space group down to 5 K and the appearance of additional Bragg reflections confirming long range magnetic ordering as measured by previous DC susceptibility measurements⁵². Since DC susceptibility measurements suggested that V^{4+} remained paramagnetic down to at least 2 K, the refinement of single crystal neutron diffraction data collected at 5 K assumed that the magnetic Bragg reflections were exclusively due to

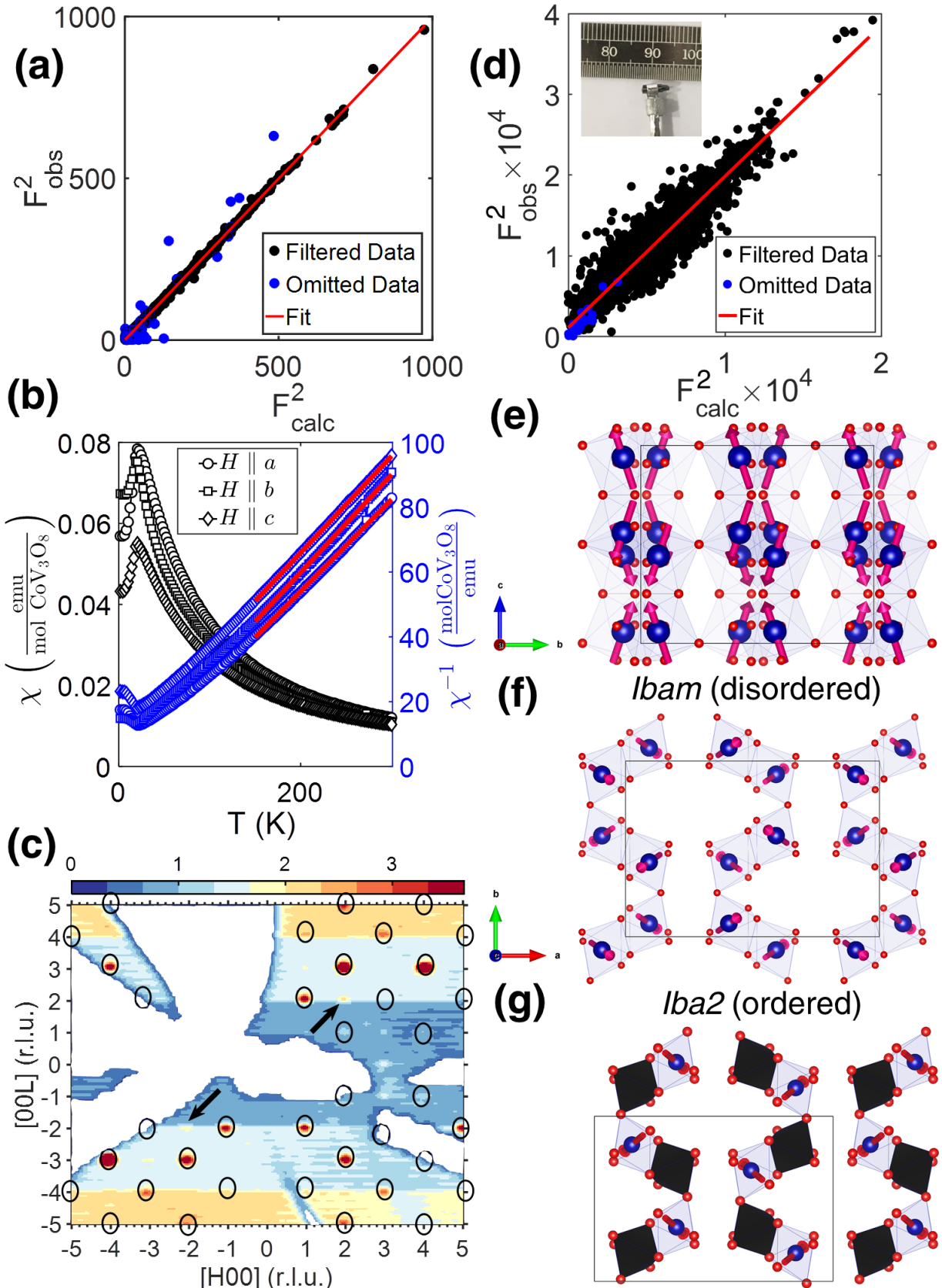


FIG. 2. (a) Refinement of single crystal x-ray diffraction data collected at 120 K yielding a refined $Ibam$ unit cell ($a=14.29344(4)$ Å, $b=9.8740(3)$ Å, $c=8.34000(3)$ Å), in agreement with previous studies⁵². (b) Temperature dependence of the DC magnetic susceptibility of α - CoV_3O_8 an external DC field $\mu_0 H_{\text{ext}} = 0.5$ T applied parallel to the three principal axes. Red lines indicate Curie-Weiss fits to high temperature data and are summarized by Tab. I. (c) Single crystal neutron diffraction intensity pattern collected at 5 K in the $(H0L)$ scattering plane. Black ellipses indicate nuclear Bragg reflections. Arrows indicate strong magnetic Bragg reflections at $(-21-2)$ and (212) . (d) Refinement of single crystal neutron diffraction data on a (inset) 0.4312 g single crystal of α - CoV_3O_8 collected at 5 K. Schematic illustration of the refined magnetic structure of α - CoV_3O_8 along the (e) bc and (f) ab planes with the Co^{2+} having 50 % occupancy. The orientation of the refined magnetic moments on Co^{2+} are indicated by red arrows. (g) illustrates the ordered $Iba2$ space group with each Co^{2+} site fully occupied and the black octahedra representing V^{4+} sites. Both panels (f) and (g) show a single layer of Co^{2+} ions.

TABLE II. Comparison of the refined magnetic moment's components assuming random (*Ibam*) and ordered (*Iba2*) distribution of Co^{2+} and V^{4+} on the metal sites of $\alpha\text{-CoV}_3\text{O}_8$. The goodness-of-fit metric χ^2 and residuals from the magnetic refinement of neutron single crystal diffraction data collected at 5 K suggests that Co^{2+} and V^{4+} are randomly distributed. Numbers in parentheses indicate statistical errors.

Parameter	Value (<i>Ibam</i>)	Value (<i>Iba2</i>)
μ_a	1.35(5) μ_B	1.30(6) μ_B
μ_b	1.16(5) μ_B	1.09(8) μ_B
μ_c	3.05(4) μ_B	2.32(5) μ_B
χ^2	3.18	5.15
R_{F2}	8.38%	10.59%
R_{wF2}	8.99%	14.57%
$R_{F2}^2_{\text{mag}}$	24.13%	32.28%

Co^{2+} that were randomly distributed throughout the 16*k* metal sites. The random distribution of Co^{2+} was accomplished by constraining the occupancy of each metal site to a value of $\frac{1}{2}$. The additional magnetic Bragg reflections were successfully indexed using a propagation vector $\mathbf{k} = (1, 1, 1)$ with the $P1ccn$ (#56.376) Shubnikov space group⁸³. The propagation vector $\mathbf{k} = (1, 1, 1)$ was initially chosen as it corresponds to the first point of symmetry reduction by removing body-centering symmetry with the same structural unit cell⁸⁴. Subsequently, utilizing the aforementioned value of \mathbf{k} , a symmetry analysis was performed in JANA2006⁶⁴. With a $\mathbf{k} = (1, 1, 1)$, the symmetry analysis considers which models were compatible — following the symmetry operations of the group, but excluding body-centering — with the restriction that moments at (x, y, z) are antiferromagnetically aligned with those moments at $(x + \frac{1}{2}, y + \frac{1}{2}, z + \frac{1}{2})$. Four models were found to be compatible, with the $P1ccn$ (#56.376) Shubnikov space group yielding the best match.

Tab. II summarizes the results of a joint nuclear and magnetic refinement utilizing 5086 out of a total of 5120 measured reflections at 5 K (Fig. 2(d)), confirming a strong preference for the $P1ccn$ Shubnikov space group of *Ibam* over $P1cc2$ of *Iba2*. The refined magnetic moment for Co^{2+} was found to be $\mu = 3.53(2) \mu_B$ with μ_a , μ_b and μ_c as 1.35(5) μ_B , 1.16(5) μ_B and 3.05(5) μ_B , respectively. $\alpha\text{-CoV}_3\text{O}_8$ adopts a magnetic structure consisting of effective pairs of 2D layers in the *ab* plane, separated from one another by a non-magnetic layer consisting of tetrahedrally coordinated V^{5+} , as illustrated in Fig. 2(f). Within these 2D layers, Co^{2+} spins are ferromagnetically coupled along both *a* and *b*, corresponding to inter-chain superexchange interactions. These 2D layers come in pairs with each offset from one another by [0.1858*a*, 0.1508*b* and 0.1194*c*] with the pair being antiferromagnetically coupled to the adjacent pair along *c*, corresponding to intra-chain superexchange interactions.

D. Inelastic Neutron Scattering

Motivated by the random distribution of Co^{2+} and V^{4+} , multiple ferro-/antiferromagnetic interactions and the presence of strong spin-orbit coupling, the spin dynamics of $\alpha\text{-CoV}_3\text{O}_8$ was investigated with inelastic neutron scattering. All inelastic scattering intensities were normalized to absolute units using the paramagnetic approximation⁸⁵. Normalization was performed by using

both Co and V as internal incoherent standards^{86,87} to calculate an absolute calibration constant \mathcal{A} converting vanadium-corrected scattering intensities $\tilde{I}(\mathbf{Q}, E)$ to the differential scattering cross section $\frac{d^2\sigma}{dE d\Omega}$ which was then converted to the dynamic structure factor $S(\mathbf{Q}, E)$ by

$$\mathcal{A}\tilde{I}(\mathbf{Q}, E) \equiv \frac{d^2\sigma}{dE d\Omega} = \left(\frac{\gamma r_o}{2}\right)^2 g_J^2 |f(\mathbf{Q})|^2 S(\mathbf{Q}, E), \quad (1)$$

where it is understood⁸⁸ that $S(\mathbf{Q}, E)$ is $S^{zz}(\mathbf{Q}, E) = \frac{\text{Tr}\{S^{\alpha\beta}(\mathbf{Q}, E)\}}{3}$, $\left(\frac{\gamma r_o}{2}\right)^2$ and g_J equals to 73 mb sr⁻¹ and the Landé *g*-factor, respectively, while the factor of 2 corresponds to the paramagnetic cross section^{85,87,89,90}. The value for the Landé *g*-factor is discussed in Appendix B 2. Hereafter, all neutron scattering quantities with a tilde (for example $\tilde{S}(|\mathbf{Q}|, E)$), denote the inclusion of the magnetic form factor squared $|f(\mathbf{Q})|^2$.

1. Spin-Orbit Transitions

As discussed in Appendix B 1, Co^{2+} ($L = 3$ and $S = \frac{3}{2}$) in an octahedral crystal field environment can be projected onto a ground state with an effective orbital angular momentum⁷⁵ of $l = 1$ with a projection factor^{60,81} α of $-\frac{3}{2}$. Diagonalizing the projected spin-orbit Hamiltonian $\hat{H}_{SO} = \alpha \hat{\mathbf{L}} \cdot \hat{\mathbf{S}}$ results in three spin-orbit manifolds^{91–93} characterized by an effective angular momentum $\hat{\mathbf{j}} = \hat{\mathbf{L}} + \hat{\mathbf{S}}$ with eigenvalues $j \equiv j_{\text{eff}}$ of $\frac{1}{2}$, $\frac{3}{2}$, and $\frac{5}{2}$. The $j_{\text{eff}} = \frac{3}{2}$ and $\frac{5}{2}$ manifolds are separated in energy from the $j_{\text{eff}} = \frac{1}{2}$ ground state doublet manifold by $\frac{3}{2}\alpha\lambda$ and $\frac{5}{2}\alpha\lambda$, respectively⁷⁵. For pure CoO ⁹¹, $|\alpha\lambda| \sim 24$ meV, and therefore for an undistorted octahedra, one would expect a crystal field excitation at ~ 36 meV. In this section, we study the magnetic excitations in $\alpha\text{-CoV}_3\text{O}_8$ in order to determine if its ground state can be considered as a $j_{\text{eff}} = \frac{1}{2}$.

Given that only small single crystals were available of $\alpha\text{-CoV}_3\text{O}_8$, preliminary neutron inelastic scattering data failed to produce a measurable signal. To extract information on the low temperature magnetic dynamics, we therefore used powders and time-of-flight neutron spectroscopy techniques. Neutron inelastic scattering measurements (Figs. 3(a)-(c)) on polycrystalline $\alpha\text{-CoV}_3\text{O}_8$ with an $E_i = 150, 60$ and 15 meV, respectively at 5 K revealed two clear low $|\mathbf{Q}|$ excitations at ~ 5 meV and ~ 25 meV. To prevent any weak magnetic signal of interest from being masked by strong phonon bands, a scaled inelastic scattering spectrum $\tilde{\gamma}S(|\mathbf{Q}|, E)$ of an approximate isostructural compound $\alpha\text{-ZnV}_3\text{O}_8$ ⁵³ collected with identical experimental conditions was subtracted as a background⁹⁴. Neutron inelastic scattering investigations of $\alpha\text{-ZnV}_3\text{O}_8$ on MARI found no evidence of correlated V^{4+} moments over the energy range reported here. The scaling factor $\tilde{\gamma}$ for the background was calculated from the ratio between energy-integrated cuts of $\tilde{S}(|\mathbf{Q}|, E)$ of $\alpha\text{-CoV}_3\text{O}_8$ and $\alpha\text{-ZnV}_3\text{O}_8$ along $|\mathbf{Q}|$ at high $|\mathbf{Q}|$, thereby normalizing by the phonon scattering. The use of $\alpha\text{-ZnV}_3\text{O}_8$ as a background not only removes the constant and $|\mathbf{Q}|^2$ -dependent background contributions but the presence of V^{4+} in both compounds allows for the isolation of magnetic fluctuations solely attributable to Co^{2+} . As illustrated in Figs. 3(d)-(g), the use of $\alpha\text{-ZnV}_3\text{O}_8$ as an effective background revealed that the ori-

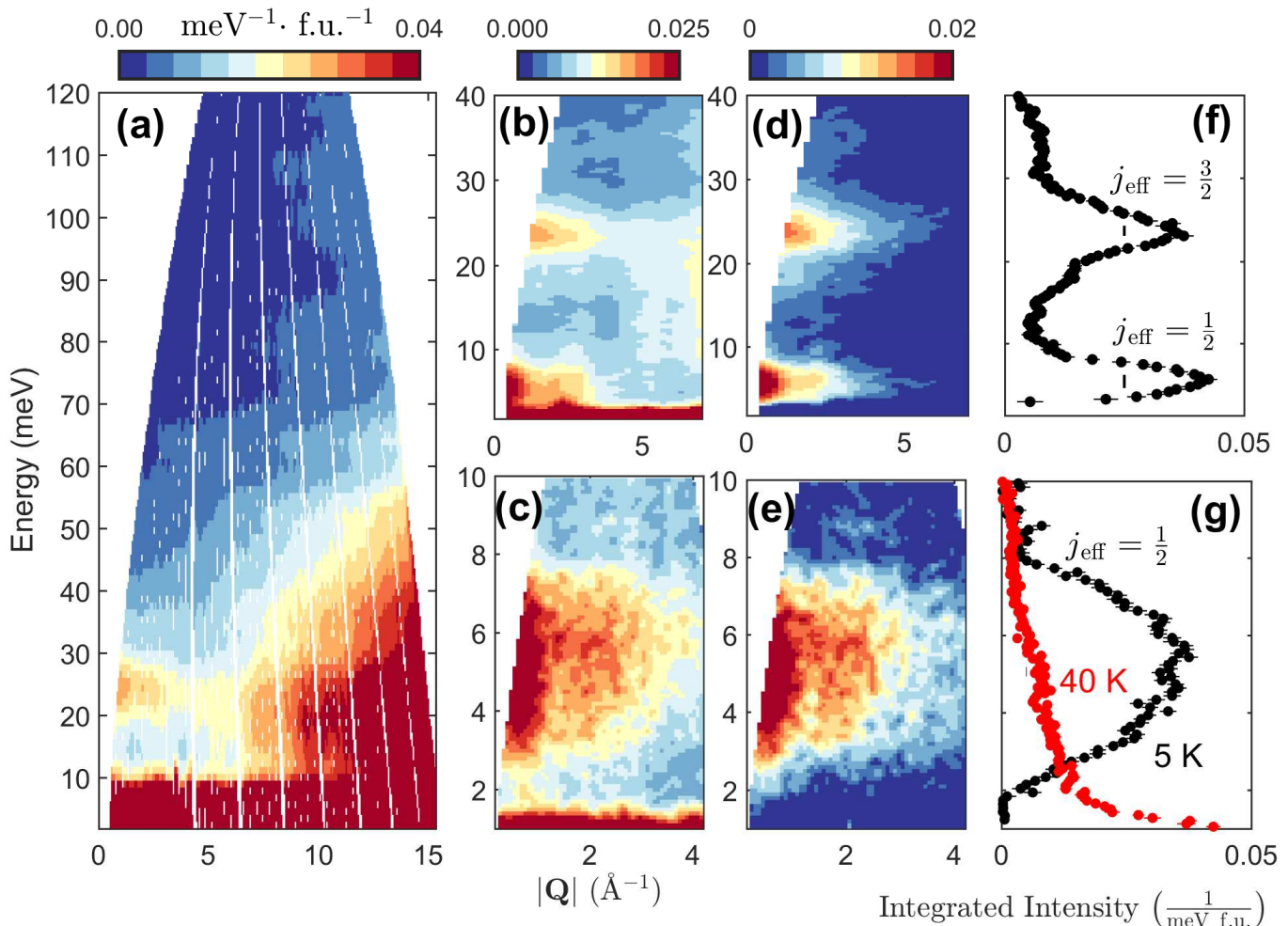


FIG. 3. $\tilde{S}(|\mathbf{Q}|, E)$ measured on MARI at $T = 5$ K with an E_i of (a) 150 meV, (b) 60 meV and (c) 15 meV. (d,e) Magnetic scattering $\tilde{S}_M(|\mathbf{Q}|, E)$ and (f,g) corresponding $|\mathbf{Q}|$ -integrated cuts ($|\mathbf{Q}|=[0,3] \text{ \AA}^{-1}$). Vertical lines in (f,g) indicate instrumental resolution. $\tilde{S}_M(|\mathbf{Q}|, E)$ was calculated by the subtraction of corresponding $\tilde{S}(|\mathbf{Q}|, E)$ for $\alpha\text{-ZnV}_3\text{O}_8$ measured at identical experimental conditions. All inelastic scattering intensities have been normalized to absolute units.

gin of the low- $|\mathbf{Q}|$ excitations must be due to Co^{2+} exclusively, excluding the possibility of any contribution from V^{4+} .

Following the analysis of inelastic scattering measurements on monoclinic and triclinic polymorphs of CoV_2O_6 ⁶⁰, the low- $|\mathbf{Q}|$ excitations in $\alpha\text{-CoV}_3\text{O}_8$ can be understood as transitions between different spin-orbit manifolds. A comparison between the inelastic spectra of CoV_2O_6 and $\alpha\text{-CoV}_3\text{O}_8$ suggests that the excitations at ~ 5 meV and ~ 25 meV are due to transitions within the $j_{\text{eff}} = \frac{1}{2}$ manifold and between the $j_{\text{eff}} = \frac{1}{2}$ and $j_{\text{eff}} = \frac{3}{2}$ manifolds, respectively. In $\alpha\text{-CoV}_3\text{O}_8$, these modes appear much broader than in CoV_2O_6 ; this will be discussed later. Such an assignment is supported by the observation that the transition at ~ 5 meV is gapped at 5 K in the magnetically ordered regime, as illustrated in Figs. 5(a) and (b). Such a gap would be a consequence of the Zeeman splitting of the $j_{\text{eff}} = \frac{1}{2}$ manifold due to the internal molecular field caused by long range ordering in the Néel phase⁶⁰. Once the temperature is raised above T_N , the molecular field would be significantly reduced due to the loss of magnetic order, resulting in the disappearance of a gap, as is experimentally observed in Fig. 3(g).

In the context of this assignment in terms of j_{eff} spin-orbit split manifolds, a difference between $\alpha\text{-CoV}_3\text{O}_8$ and

monoclinic $\alpha\text{-CoV}_2\text{O}_6$ is the absence of an observable ~ 110 meV magnetic excitation (Fig. 3(a)). As was previously calculated for CoV_2O_6 ⁶⁰, in addition to the strong excitations for the intra- $j_{\text{eff}} = \frac{1}{2}$ and the $j_{\text{eff}} = \frac{1}{2}$ to $j_{\text{eff}} = \frac{3}{2}$ transitions, the intensity of the $j_{\text{eff}} = \frac{1}{2}$ to $j_{\text{eff}} = \frac{5}{2}$ transition scales with the distortion of the local coordination octahedra^{95,96} with the transition being absent for a perfect octahedra like in rocksalt and cubic CoO ⁹¹. The distortion of the local octahedra can be quantified by the parameter δ defined by

$$\delta = \frac{1}{\mathcal{N}} \sum_i \left\{ \left(\frac{d_i - \langle d \rangle}{\langle d \rangle} \right)^2 \times 10^4 \right\}, \quad (2)$$

where $\mathcal{N} = 6$ and $\langle d \rangle$ denotes the average distance^{60,97}. $\alpha\text{-CoV}_3\text{O}_8$ exhibits a much weaker octahedral distortion ($\delta = 11.106(8)$) than $\alpha\text{-CoV}_2\text{O}_6$ ($\delta = 55$) and is thus expected to have a significantly weaker intensity. This is also in agreement with previous results on triclinic $\gamma\text{-CoV}_2\text{O}_6$ (with $\delta = 2.1$ and 4.8 for the two different Co^{2+} sites) which failed to observe a $j_{\text{eff}} = \frac{5}{2}$ transition⁶⁰. A distortion of the local octahedra around the Co^{2+} site should result in an anisotropic term in the magnetic Hamiltonian^{96,98,99}. Given the powder average na-

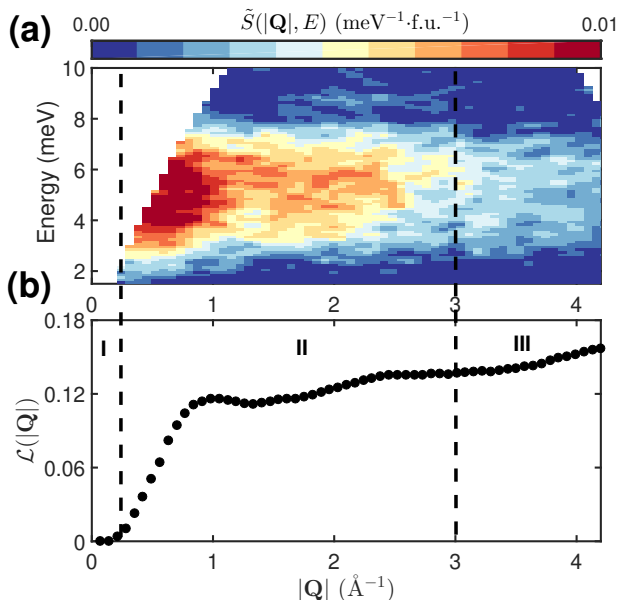


FIG. 4. (a) Magnetic scattering $\tilde{S}_M(|\mathbf{Q}|, E)$ of α -CoV₃O₈ measured on MARI at T = 5 K with an E_i of 15 meV and the corresponding (b) $|\mathbf{Q}|$ -dependence of the total integrated inelastic ($E=[2,8]$ meV) magnetic scattering intensity \mathcal{L} . Regions I, II and III denote “get-lost” tube-, magnetic- and phonon/form factor-dominated regions, respectively.

ture of the dynamics (discussed below), we are not sensitive to this term. However, the consistency of the inelastic response with the j_{eff} description discussed above in terms of the energy response is also consistent with other Co²⁺-based magnets where a local distortions of the octahedra exists^{60,95}. We now discuss further evidence for our interpretation in terms of j_{eff} levels by applying the sum rules of neutron scattering to the integrated inelastic scattering intensity.

2. Total Moment Sum Rule

To confirm the assignment of the 5 meV signal as excitations within the ground state $j_{\text{eff}} = \frac{1}{2}$ manifold, the total integrated spectral weight at 5 K of the lowest lying excitation was calculated. As summarized by the total moment sum rule of neutron scattering^{87,100–103}, the sum of all spectral weight is defined by

$$\frac{3 \int d^3\mathbf{Q} \int dE S(\mathbf{Q}, E)}{\int d^3\mathbf{Q}} = j(j+1), \quad (3)$$

where $S(\mathbf{Q}, E) \equiv S^{zz}(\mathbf{Q}, E)$ denotes the magnetic component of the dynamic structure factor $\tilde{S}_M^{\tilde{z}z}(\mathbf{Q}, E)$ that has been further renormalized by $|f(\mathbf{Q})|^2$. The extra factor of 3 has been included to assure consistency with the definition of $S(\mathbf{Q}, E) \equiv S^{zz}(\mathbf{Q}, E)$ given by Eq. 1 in the paramagnetic approximation. A measurement of the integrated intensity is therefore sensitive to the effective j of the manifold of levels being integrated over. Eq. 3 can be simplified by integrating out the angular dependence and canceling common terms resulting in an integral \mathcal{L} defined by

$$\mathcal{L}(|\mathbf{Q}|) = \frac{3 \int d|\mathbf{Q}||\mathbf{Q}|^2 \int dE S(|\mathbf{Q}|, E)}{\int d|\mathbf{Q}||\mathbf{Q}|^2}, \quad (4)$$

The total integral \mathcal{L} is uniquely a function of $|\mathbf{Q}|$ and represents an integration of the magnetic density of states over all energies including both elastic and inelastic channels in the cross section⁸⁷. With $j_{\text{eff}} = \frac{1}{2}$, the total moment sum rule (Eq. 3) would predict a value of 0.75 for the total integrated intensity.

Since the assignment discussed above based on spin-orbit transitions assumes that the ~ 5 meV excitation and the elastic cross section is exclusively due to excitations within the $j_{\text{eff}} = \frac{1}{2}$ manifold, all quantities in Eq. 3 were projected onto the ground state doublet manifold by the projection theorem of angular momentum^{93,94,104}. As discussed in Appendix B2, the projection onto the ground state doublet required defining the projected value of the Landé g -factor g_J as $g'_J = \frac{13}{3}$ and the effective angular momentum j_{eff} as $\frac{1}{2}$ ^{75,105}. As illustrated in Fig. 4, the total integrated inelastic intensity of $S(|\mathbf{Q}|, E) \equiv S^{zz}(|\mathbf{Q}|, E)$ given by $\mathcal{L}(|\mathbf{Q}|)$ (Eq. 4) saturates at 0.15(1). Combining the total integral of the inelastic contribution and an elastic contribution¹⁰⁶ of $\left(\frac{\mu}{g'_J \mu_B}\right)^2 = 0.66$, yields a total integral of 0.81 ± 0.14 , in excellent agreement with the total moment prediction for $j_{\text{eff}} = \frac{1}{2}$ of 0.75. The agreement further confirms our assignment of the low energy excitations to transitions within the ground state $j_{\text{eff}} = \frac{1}{2}$ spin-orbit doublet manifold.

With the low energy excitations being successfully approximated by pure j_{eff} manifolds, we may now rationalize the effective paramagnetic moment p_{eff} of $5.213(7) \mu_B$ that was calculated from DC susceptibility. Given that the $j_{\text{eff}} = \frac{1}{2}$ and $j_{\text{eff}} = \frac{3}{2}$ manifolds are separated by ~ 24 meV (~ 278 K), both are significantly thermally populated at the high temperatures used for the Curie-Weiss fit. In such a high temperature regime, we would expect a p_{eff} of $g_s \sqrt{S(S+1)} = 3.9 \mu_B$, which is significantly less than the measured value as has been commonly observed for other magnets based on Co²⁺ in octahedral coordination^{59,60,92,107}. The extra component measured with susceptibility may be accounted for by noting that V⁴⁺ contributes $g_s \sqrt{S(S+1)} = 1.7 \mu_B$. Therefore the addition of the contributions to p_{eff} from both Co²⁺ and V⁴⁺ corresponds to a total predicted $p_{\text{eff}} = 5.6 \mu_B$, in close agreement with the experimental data, with the small discrepancy potentially attributable to the fact that the $j_{\text{eff}} = \frac{5}{2}$ manifold is still not significantly populated at T \sim 300 K. Although it is worth noting that an additional and distinct possibility for a much larger measured effective paramagnetic moment may be a strong orbital contribution as has been observed for the case of CoO^{108,109}, where the orbital contribution is significant, corresponding to approximately $\frac{1}{3}$ of the total ordered moment.

E. Critical Exponents

Despite the similarities between the inelastic spectra of α -CoV₃O₈ and CoV₂O₆, one difference is the bandwidth of the low energy excitation that we have assigned to the $j_{\text{eff}} = \frac{1}{2}$ manifold. As illustrated in Fig. 3(g), in contrast

to both polymorphs of CoV_2O_6 , $\alpha\text{-CoV}_3\text{O}_8$ exhibits a broad peak in energy whose bandwidth is approximately 20 times that of instrumental resolution. Such a large bandwidth could be accounted for by magnetic exchange coupling between spins^{60,110,111}. However, an alternative explanation may lie in the intrinsic cationic disorder inherent to the disordered *Ibam* structure of $\alpha\text{-CoV}_3\text{O}_8$ ⁵². Such large cationic disorder would result in a distribution of cationic sites and correspondingly a spread of spin-orbit transitions as has been shown for multiple doped systems^{46,49,112–116}, and thus perhaps such disorder may also explain the large bandwidth in $\alpha\text{-CoV}_3\text{O}_8$ due to a distribution of molecular fields splitting the $j_{\text{eff}} = \frac{1}{2}$ manifold. We investigate this possibility in this section using scaling.

1. Scaling Analysis

The presence of such disorder would result in temperature being the dominant energy scale. To investigate this possibility, the temperature dependence of the Co^{2+} spin fluctuations was analyzed using a scaling analysis previously employed for the charge doped cuprates^{117–121}. For paramagnetic fluctuations, critical scattering theory assumes a single energy scale, the relaxation rate Γ , is dominant¹²². If Γ is driven by temperature, then it can be shown that the energy-temperature dependence of the uniform dynamic susceptibility $\chi''(E, T)$, follows $\frac{E}{T}$ scaling^{117,118} given by

$$\frac{\chi''(T, E)}{\chi''(T=0 \text{ K}, E)} = \arctan \left\{ \sum_{i=0} a_i \left(\frac{E}{T} \right)^{2i+1} \right\}, \quad (5)$$

where $\chi''(T=0 \text{ K}, E)$ denotes the value of χ'' in the limit of $T = 0 \text{ K}$ and all even powers are excluded in the sum to satisfy detailed balance, requiring χ'' to be an odd function of energy¹²⁰. For this particular analysis, the value of $\chi''(T, E)$ was calculated by first subtracting a temperature independent background from the measured $S(T, |\mathbf{Q}|, E)$. The contribution of the background was determined by an algorithm previously employed for $\text{Fe}_{1+x}\text{Te}_{0.7}\text{Se}_{0.3}$ ¹²³ and polymer quantum magnets¹²⁴. The algorithm is based on the requirement that all inelastic scattering must obey detailed balance accounting for both sample environment and other temperature-independent scattering contributions, and thus isolating the fluctuations exclusively due to Co^{2+} . The background-subtracted dynamic structure factor was then converted to $\chi''(T, |\mathbf{Q}|, E)$ via the fluctuation-dissipation theorem¹²⁵

$$\chi''(T, |\mathbf{Q}|, E) = g^2 \mu_B^2 \pi \left\{ \frac{1}{n(E, T) + 1} \right\} S(T, |\mathbf{Q}|, E), \quad (6)$$

where $n(E, T)$ is the Bose factor. Finally, $\chi''(T, |\mathbf{Q}|, E)$ was integrated over $|\mathbf{Q}| = [0, 3]$ and $[0, 2] \text{ \AA}^{-1}$ for measurements on MARI and IRIS, respectively. As illustrated in Fig. 5(c), $\frac{E}{T}$ scaling adequately accounts for the experimental data with the need for only two refined constants of 3.2(1) and 0.8(2) for a_0 and a_2 , respectively, since the inclusion of higher order terms in Eq. 5 did not improve the fit. The success of $\frac{E}{T}$ scaling suggests that

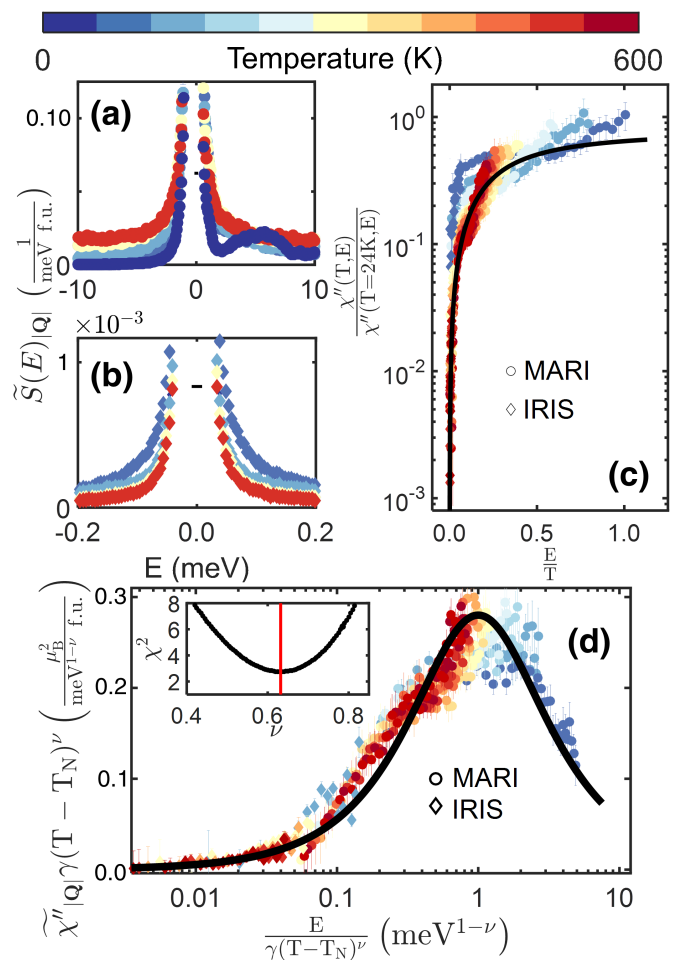


FIG. 5. $|\mathbf{Q}|$ -integrated cuts of $\tilde{S}(|\mathbf{Q}|, E)$ measured on (a) MARI and (b) IRIS at various temperatures. Horizontal lines indicate instrumental resolution. (c) Energy and temperature dependence of the normalized χ'' calculated from $|\mathbf{Q}|$ -integrated cuts of $\tilde{S}_M(|\mathbf{Q}|, E)$ measured on both IRIS at MARI. (d) Compilation of the energy-temperature dependence of $|\mathbf{Q}|$ -integrated χ'' as calculated in (c). As discussed in the main text, the data is described by a Lorentzian relaxation form (Eq. 8), revealing scaling behavior consistent with $\Gamma \propto (T - T_N)^\nu$. The line of best fit yields $\nu = 0.636(10)$, corresponding to a global minimum of χ^2 as illustrated in the inset. All panels share the same temperature scale (top horizontal intensity bar). All $|\mathbf{Q}|$ -integrated cuts on MARI and IRIS are from $|\mathbf{Q}| = [0, 3] \text{ \AA}^{-1}$ for $E_i = 15 \text{ meV}$ and from $|\mathbf{Q}| = [0, 2] \text{ \AA}^{-1}$ for $E_f = 1.84 \text{ meV}$, respectively.

$\Gamma \propto T^\nu$ and the larger value of a_0 over all other terms suggests $\nu \leq 1$.

The value of ν was refined using a modified scaling algorithm previously employed to detect anomalous scaling in the vicinity of a quantum critical point for CeCu_2Si_2 and $\text{CeCu}_{6-x}\text{Au}_x$ ^{126–128}. Utilizing the single relational energy mode approximation and the Kramers-Kronig relations¹²⁹, the uniform dynamic susceptibility can be approximated as a Lorentzian-like response^{95,117,130–135} given by

$$\chi'' = \chi' \left\{ \frac{E\Gamma}{E^2 + \Gamma^2} \right\}, \quad (7)$$

where χ' denotes the static susceptibility and $\Gamma \propto \xi^{-1}$, where ξ is the correlation length¹³⁶. If one assumes both

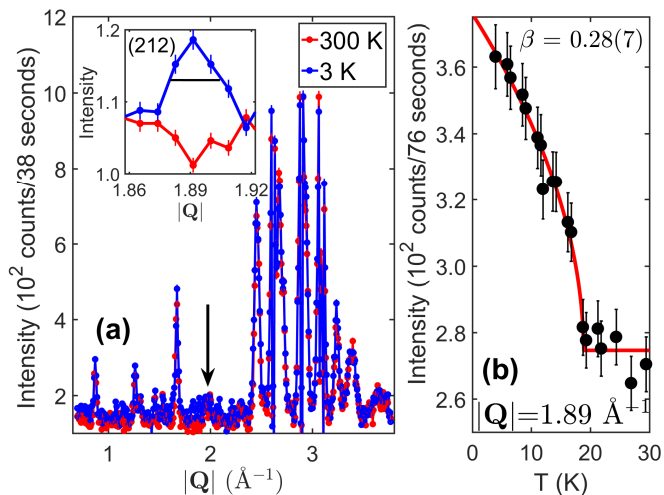


FIG. 6. (a) Neutron diffraction profiles of polycrystalline α - CoV_3O_8 collected at 3 and 300 K on BT4. (inset) Additional scattering intensity on the (212) magnetic Bragg reflection at 3 K confirms long range magnetic order. The horizontal line indicates instrumental resolution. (b) Temperature dependence of the elastic intensity at $|\mathbf{Q}| = 1.89 \text{ \AA}^{-1}$ ($2\theta = 41.6^\circ$), corresponding to the maximum of the (212) magnetic Bragg reflection as indicated by the arrow in (a). A fit to $(T_N - T)^{2\beta}$ yields $T_N = 18.8(6) \text{ K}$ and $\beta = 0.28(7)$.

the single energy scale $\Gamma = \gamma(T - T_N)^\nu$ and the static susceptibility $\chi' = \frac{C}{\Gamma}$, where γ and C are constants, then Eq. 7 assumes the form

$$\chi'' = \frac{C}{\gamma(T - T_N)^\nu} \left\{ \frac{\frac{E}{\gamma(T - T_N)^\nu}}{1 + \left(\frac{E}{\gamma(T - T_N)^\nu}\right)^2} \right\}. \quad (8)$$

The first assumption leading to Eq. 8 stems from the fact that the scaling properties of the dynamics are being investigated near the vicinity of an ordering transition at $T_N \sim 19 \text{ K}$ and not a quantum critical point as in the cuprates and heavy fermion systems^{106,128,137}, a fact that was reflected in Fig. 5(c) by defining $\chi''(T = 0, E)$ as the value at 24 K. The second assumption is based on the paramagnetic behavior observed with DC susceptibility at high temperatures, suggesting χ' should adopt a Curie-Weiss form^{106,117}. As illustrated in Fig. 5(d), the scaling relation (Eq. 8) provides a good description of the experimental data over 4 orders of magnitude in $\frac{E}{T}$, yielding a refined ν of 0.636(10). It is important to note that the refined value of ν is not consistent with random dilute 3D Ising behavior where $\nu = 0.683(2)$, but instead is consistent with the ordered 3D Ising universality class with a $\nu = 0.6312(3)$ ^{122,138-142}. While scaling and critical scattering typically only applies near the phase transition, work on other transition metal based compounds has found critical scattering that scales up to high temperatures in the paramagnetic regime^{110,143}.

2. Magnetic Order Parameter

The scaling analysis in the previous section found that the critical fluctuations are both consistent with an ordered three dimensional Ising universality class and with

the DC susceptibility data presented above. Consequently, while the excitations are separated into distinct j_{eff} manifolds, the scaling analysis indicates that the distortion does introduce an anisotropy term in the magnetic Hamiltonian influencing the critical dynamics outlined in the previous section. In an attempt to further deduce the universality class of CoV_3O_8 , neutron diffraction measurements were performed on polycrystalline α - CoV_3O_8 to extract further critical exponents. As illustrated in Fig. 6(a), polycrystalline α - CoV_3O_8 exhibits long range magnetic ordering at 3 K, in agreement with both single crystal DC susceptibility (Fig. 2(b)) and single crystal neutron diffraction (Fig. 2(c)) measurements. The temperature dependence of the scattering intensity of the (212) magnetic Bragg reflection is displayed in Fig. 6(b), corresponding to the square of the magnetic order parameter¹⁴⁴ ϕ , given by the power-law dependence

$$I(T) \equiv \phi^2(T) \propto (T_N - T)^{2\beta}, \quad (9)$$

yields a refined T_N of 18.8(6) K in agreement with DC susceptibility measurements and a refined β of 0.28(7). Although the value of β is in agreement with the predicted value of 0.326 for the ordered 3D Ising universality class¹²², the large statistical error also implies agreement with the predicted value for the random dilute 3D Ising model of 0.35¹³⁸⁻¹⁴¹. Therefore, the critical magnetic fluctuations are in agreement with expectations from both ordered and disordered 3D Ising behavior.

F. First Moment Sum Rule, Local Cation Ordering & Single Mode Approximation

In order to deduce further information concerning both the dimensionality d and the microscopic exchange constants J , a combination of the first moment sum rule of neutron scattering and the single mode approximation was employed. The determination of the values for J and d begin with the Hohenberg-Brinkman first moment sum rule¹⁴⁵ given by

$$\begin{aligned} \langle E \rangle(\mathbf{Q}) &= \int dE E S(\mathbf{Q}, E) \\ &= -\frac{2}{3} \sum_{i,j} n_{ij} J_{ij} \langle \hat{\mathbf{S}}_i \cdot \hat{\mathbf{S}}_j \rangle (1 - \cos(\mathbf{Q} \cdot \mathbf{d}_{ij})) \end{aligned} \quad (10)$$

and its powder-average

$$\langle E \rangle(|\mathbf{Q}|) = -\frac{2}{3} \sum_{i,j} n_{ij} J_{ij} \langle \hat{\mathbf{S}}_i \cdot \hat{\mathbf{S}}_j \rangle \left\{ 1 - \frac{\sin(|\mathbf{Q}||\mathbf{d}_{ij}|)}{|\mathbf{Q}||\mathbf{d}_{ij}|} \right\}, \quad (11)$$

as derived in Appendix C, where n_{ij} , J_{ij} , $\langle \hat{\mathbf{S}}_i \cdot \hat{\mathbf{S}}_j \rangle$ and \mathbf{d}_{ij} denote the number of individual exchange interactions, the exchange constant, the spin-spin correlator and the displacement vector between spins at sites i and j , respectively^{60,102,146}.

Since all of the inelastic intensity measured at 5 K on MARI with an $E_i = 15 \text{ meV}$ shown in Fig. 3(g) corresponds to excitations within the ground state $j_{\text{eff}} = \frac{1}{2}$, proven by the total moment sum rule, then the single mode approximation (SMA) can be applied^{102,147}.

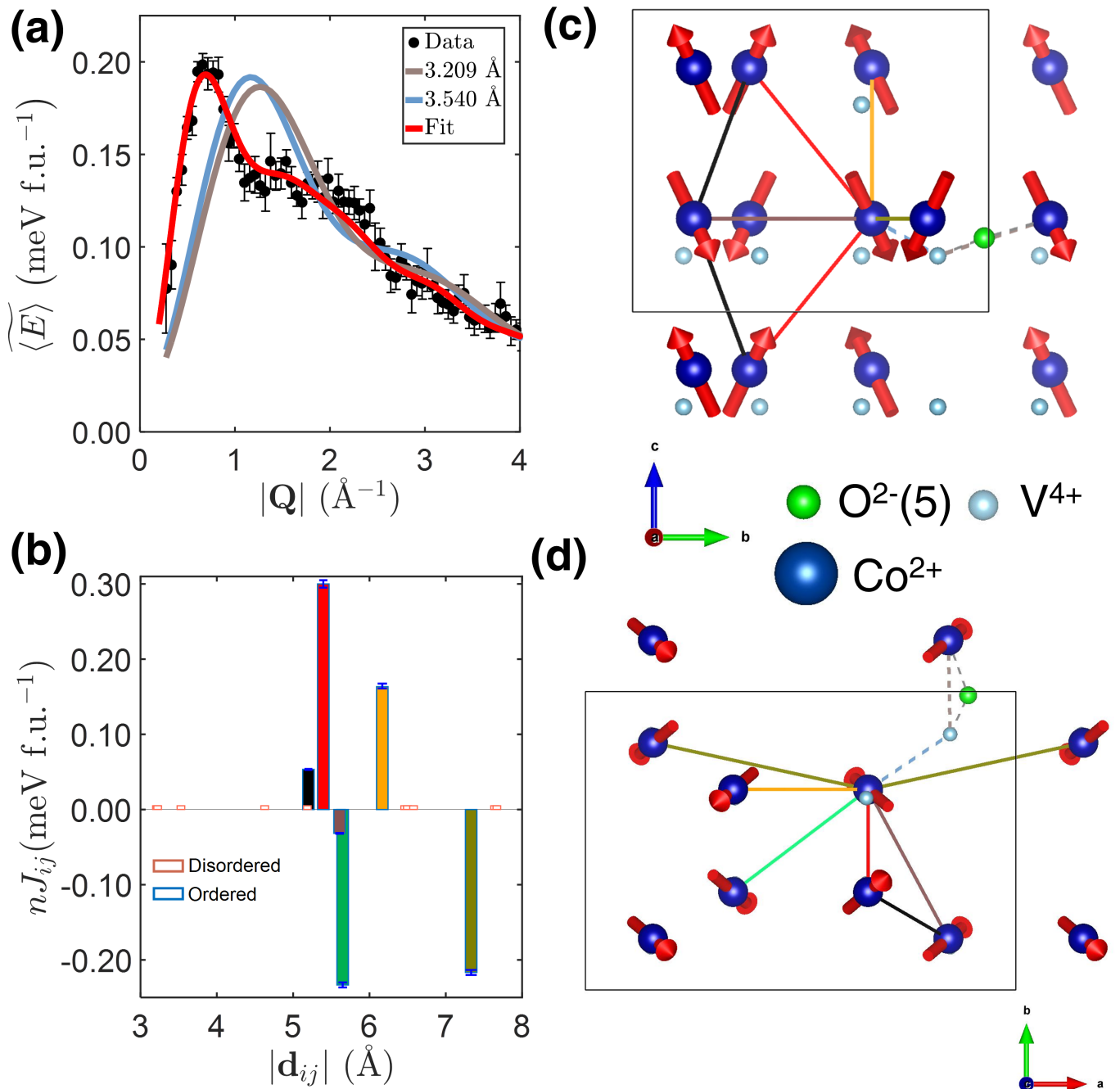


FIG. 7. (a) $|\mathbf{Q}|$ -dependence of the background subtracted first moment $\langle \widetilde{E} \rangle$ as measured on MARI at $T=5$ K with an $E_i=15$ meV integrated over $E=[2,8]$ meV. A fit to the first moment sum rule (Eq. 11) reveals that only six distances $|\mathbf{d}_{ij}|$ out to 7.5 Å possess non-negligible nJ_{ij} values as illustrated in (b), and summarized in Tab. III. For the purposes of comparison, distances present only in the ordered and disordered atomic arrangements are distinguished by purple and dark pink outline colors, respectively. Distances with non-negligible nJ_{ij} contributions have a face color corresponding to the illustration of the corresponding six interactions along the (c) bc and (d) ac planes of the α -CoV₃O₈ unit cell. Both non-bridging oxygen atoms have been excluded and V⁴⁺ ions have been reduced in size for the purposes of clarity. Two particular distances: 3.209 Å and 3.540 Å are absent as noted in (a), corresponding to nearest neighbor and bridging metal site distances, respectively.

The single mode approximation, applicable to a situation where the excitation spectrum is dominated a single coherent mode, allows for the dynamic structure factor to be written as $S(\mathbf{Q}, E) = S(\mathbf{Q})\delta[\epsilon(\mathbf{Q}) - E]$, where $\delta[\epsilon(\mathbf{Q}) - E]$ assures energy conservation^{60,87,100,124,148}. Applying the single mode approximation to the first moment sum rule yields

$$S(\mathbf{Q}, E) = -\frac{2}{3} \frac{1}{\epsilon(\mathbf{Q})} \sum_{i,j} n_{ij} J_{ij} \langle \hat{\mathbf{S}}_i \cdot \hat{\mathbf{S}}_j \rangle \{1 - \cos(\mathbf{Q} \cdot \mathbf{d}_{ij})\} \delta[\epsilon(\mathbf{Q}) - E], \quad (12)$$

providing a quantitative relationship between $S(\mathbf{Q}, E)$ and the dispersion $\epsilon(\mathbf{Q})$ and by extension, a measure of the dimensionality^{60,87,149,150}. For numerical purposes, the delta function was approximated as a Lorentzian with

a FWHM equal to that of the calculated experimental resolution width of 0.24 meV at 5 meV transfer on MARI. Eqs. 10-12 assume the presence of Heisenberg exchange and thus excludes exchange anisotropy^{60,100,102,147}. It is important to note that the exclusion of any anisotropy terms is simply a first approximation based on the success of the isotropic exchange model to account for experimental data in a variety of other Co²⁺-based systems such as CoV₂O₆, KMn_{1-x}Co_xF₃ and Mn_{1-x}Co_xF₂^{13,60,92,105,151}. In fact, there is evidence that anisotropic exchange is not negligible in α -CoV₃O₈. Such experimental evidence includes equal intensities for transitions within the ground state manifold and between the ground state and first excited state manifolds^{75,92}, as illustrated in Fig. 3(f). Another piece of evidence is the presence of a weak signal at ~ 1 meV at low energy transfer measurements, as illustrated in Fig. 3(g) that may be indicative of anisotropic breakdown of magnetic excitations^{60,75,87,100,152}. The non-negligible value of anisotropic exchange in α -CoV₃O₈ is indeed expected due to the distorted octahedra around Co²⁺ ($\delta \sim 11$) and has been observed in α, γ -CoV₂O₆ with similar distortion parameters^{60,82} but will be excluded in the context of the current discussion.

1. First Moment Sum Rule & Cation Order

This section utilizes the first moment sum rule of neutron scattering to provide an estimate of the exchange constants in α -CoV₃O₈. Fig. 7(a) shows the background subtracted first moment $\langle E \rangle(|\mathbf{Q}|)$ at 5 K was successfully described by the powder averaged first moment sum rule (Eq. 11) incorporating all possible 15 Co²⁺-Co²⁺ distances in the α -CoV₃O₈ unit cell from $|\mathbf{d}_{ij}| = [3.209, 7.669]$ Å. As summarized by Tab. III, a least squares optimization revealed that only six unique distances possess non-negligible $-n_{ij}J_{ij}\langle \hat{\mathbf{j}}_i \cdot \hat{\mathbf{j}}_j \rangle$ values, where the use of $\hat{\mathbf{j}}$ in the correlator instead of $\hat{\mathbf{S}}$ is due to the use of g'_j in the normalization process. Two particular distances with negligible $-n_{ij}J_{ij}\langle \hat{\mathbf{j}}_i \cdot \hat{\mathbf{j}}_j \rangle$ contributions are 3.209 Å and 3.540 Å, corresponding to the nearest neighbor and metal site distances across the O(5) bridging ligand, respectively. The absence of the latter is expected due to the local selection rule⁵² as illustrated in Fig. 1(c), but the absence of the nearest neighbor distance is inconsistent with a random distribution of Co²⁺ inherent to the disordered *Ibam* structure previously deduced by diffraction measurements that are summarized in Fig. 2. Upon closer inspection of the α -CoV₃O₈ unit cell, these six distances were shown to correspond to the unique distances found exclusively in the ordered *Iba2* structure⁵³ as illustrated in Figs. 7(c) and (d), confirming an ordered arrangement of Co²⁺.

While this analysis indicates the distances are consistent with the ordered *Iba2* structure, there are two potential caveats. Because we measure the product $-n_{ij}J_{ij}\langle \hat{\mathbf{j}}_i \cdot \hat{\mathbf{j}}_j \rangle$, (i) the value of n_{ij} may not be negligible but instead it may be the correlator $\langle \hat{\mathbf{j}}_i \cdot \hat{\mathbf{j}}_j \rangle$ whose value is negligible; (ii) and/or the exchange constants J_{ij} may themselves be negligible. To address issue (i), we have calculated the correlator $\langle \hat{\mathbf{j}}_i \cdot \hat{\mathbf{j}}_j \rangle$ based on energy-integrated magnetic diffraction data (Tab. III) and found

TABLE III. Distances $|\mathbf{d}_{ij}|$ with corresponding non-negligible refined values of $-n_{ij}J_{ij}\langle \hat{\mathbf{j}}_i \cdot \hat{\mathbf{j}}_j \rangle$ and $n_{ij}J_{ij}$ from the fit of the first moment $\langle E \rangle(|\mathbf{Q}|)$ ($E=[2,8]$ meV) at 5 K to the first moment sum rule¹⁴⁵. The corresponding calculated spin-orbit corrected Curie-Weiss constant $\bar{\theta}_{CW}$ (Eq. 13) is in close agreement with the experimentally determined Curie-Weiss constant averaged over all three principal directions $\bar{\theta}_{CW, \text{exp}}$. Numbers in parentheses indicate statistical errors.

$ \mathbf{d}_{ij} $ (Å)	$-n_{ij}J_{ij}\langle \hat{\mathbf{j}}_i \cdot \hat{\mathbf{j}}_j \rangle$ (meV f.u. ⁻¹)	$\langle \hat{\mathbf{j}}_i \cdot \hat{\mathbf{j}}_j \rangle$	$n_{ij}J_{ij}$ (meV f.u. ⁻¹)
5.200(2)	0.023(1)	-0.420(2)	0.055(1)
5.395(3)	0.173(1)	-0.594(3)	0.30(1)
5.6083(14)	0.016(2)	0.484(2)	-0.033(1)
5.649(4)	0.099(2)	0.417(3)	-0.24(1)
6.168(3)	0.08(1)	-0.483(3)	0.17(1)
7.3321(9)	0.13(1)	0.595(4)	-0.22(1)
$\bar{\theta}_{CW, \text{exp}}$	-3.2(4) K		
$\bar{\theta}_{CW}$	-0.24(15) K		

it to be substantial for all distances. We address argument (ii) by pointing out that some distances with negligible $-n_{ij}J_{ij}\langle \hat{\mathbf{j}}_i \cdot \hat{\mathbf{j}}_j \rangle$ have a Co²⁺-O²⁻-Co²⁺ angle close to 180°, predicted by the Goodenough-Kanamori-Anderson rules to yield strong antiferromagnetic exchange⁷⁶⁻⁷⁸.

We now extract the exchange constants J_{ij} by dividing out the correlator from the $-n_{ij}J_{ij}\langle \hat{\mathbf{j}}_i \cdot \hat{\mathbf{j}}_j \rangle$. By inserting the 6 values of $n_{ij}J_{ij}$ in the mean field expression for the Curie-Weiss temperature^{153,154}

$$\bar{\theta}_{CW} = -\frac{S(S+1)\sum_{i,j}n_{ij}J_{ij}}{3\zeta}, \quad (13)$$

where ζ is a scale factor of 1.9 calculated by Kanamori⁸¹, one obtains -0.24(15) K, a value that is both small and negative, in agreement with the experimentally determined value of -3.2(4) K. The close similarity between the calculated and experimentally determined values of θ_{CW} suggests that all relevant exchange interactions have been accounted for by the *Iba2* structure. It is important to emphasize that this analysis assumes isotropic exchange and thus assumes the isotropic part of the magnetic Hamiltonian is dominant. While susceptibility data indicates some anisotropy, the similarity between the extracted exchange constants and the θ_{CW} lends support for the isotropic approximation, while the slightly larger negative measured value may possibly be indicative of some anisotropic contributions. Future advances in both single crystal growth of this material and also higher flux neutron instrumentation will allow single crystal data to be obtained and the parameters refined.

2. Single Mode Approximation & Dimensionality

Since the first moment sum rule indicates the presence of multiple unique interactions spanning all three crystallographic directions in the *Iba2* structure⁵³, it was suspected that a more intricate dispersion relation should be chosen for Eq. 12, such as the expression given by

TABLE IV. Refined parameters of the heuristic dispersion relation in the single mode approximation of $\tilde{S}(|\mathbf{Q}|, E)$ utilizing the refined values of $-n_{ij}J_{ij}\langle\hat{\mathbf{S}}_i \cdot \hat{\mathbf{S}}_j\rangle$ at 5 K summarized in Tab. III. As a first approximation, the intra-plane dispersion parameters were fixed to zero. Numbers in parentheses indicate statistical errors.

Dispersion Parameter	Refined Value (meV ²)
B_o	28.2(3)
B_h	-1.13(2)
B_k	-4.63(4)
B_l	6.8(7)
B_{hk}	0
B_{hl}	0
B_{kl}	0
B_{2h}	-1.13(2)
B_{2k}	-4.63(4)
B_{2l}	6.8(7)

$$\begin{aligned} \epsilon(\mathbf{Q}) = & (B_o + B_h \cos(2\pi h) + B_k \cos(2\pi k) + B_l \cos(2\pi l) \\ & + B_{hk} \{\cos[2\pi(h+k)] + \cos[2\pi(h-k)]\} \\ & + B_{hl} \{\cos[2\pi(h+l)] + \cos[2\pi(h-l)]\} \\ & + B_{kl} \{\cos[2\pi(k+l)] + \cos[2\pi(k-l)]\} \\ & + B_{2h} \cos(4\pi h) + \beta_{2k} \cos(4\pi k) + B_{2l} \cos(4\pi l))^{\frac{1}{2}}, \end{aligned} \quad (14)$$

where B_i are the dispersion parameters. The dispersion relation $\epsilon(\mathbf{Q})$ in Eq. 14 satisfies Bloch's theorem⁸⁹ and has been previously used to parametrize the dispersion for more complex systems involving multiple exchange interaction pathways such as PHCC¹⁰⁰, whose large dispersions could not be adequately described with the heuristic model $\epsilon(\mathbf{Q}) = \beta_o + \sum_i \beta_i \cos(\mathbf{Q} \cdot \mathbf{d}_{ij})$ ^{60,124,155}.

As a first approximation, the parameters in Eq. 14 involving interactions between the principal axes were set to zero and each parameter along a particular principal axis was set to be equal (e.g. $B_h = B_{2h}$). This simple model effectively reduces Eq. 14 to the aforementioned simple heuristic model^{60,124,155} and treats every exchange interaction as a combination of interactions along the three principal axes. As illustrated in Fig. 8, all major features of $\tilde{S}_M(|\mathbf{Q}|, E)$ collected at 5 K, including the large bandwidth, was successfully accounted for by a least squares optimization of the dispersion parameters. As summarized in Tab. IV, the refined dispersion parameters indicate the presence of three dimensional magnetism, consistent with the lack of significant asymmetry in the $|\mathbf{Q}|$ -integrated cut $\tilde{S}_M(E)_{|\mathbf{Q}|}$ displayed in Fig. 8(c), as would be expected for both 1D and 2D magnetic fluctuations^{87,156,157}. As summarized by Tab. IV, the dispersion parameters along h and l are both negative while the dispersion parameters along k are positive with a larger magnitude. Both the signs and relative magnitudes of the dispersion parameters can be reconciled using the spin-flip hopping model^{60,158}, where B_i for a particular direction i is interpreted as a hopping term whose value is proportional to the energy cost of a spin-flip $t \sim SJ$ along that particular direction. The negative h and k dispersion parameters correspond to

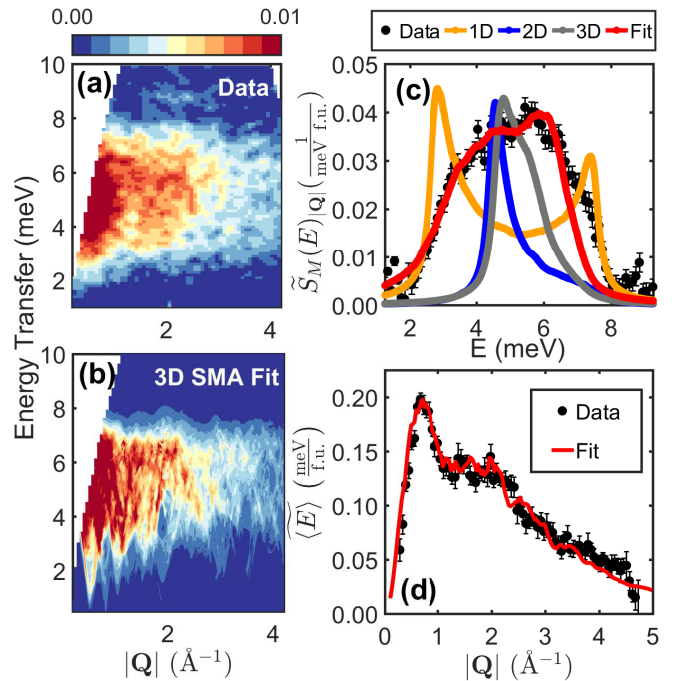


FIG. 8. (a) $\tilde{S}_M(|\mathbf{Q}|, E)$ measured on MARI at T=5 K with an $E_i=15$ meV. (b) $\tilde{S}_M(|\mathbf{Q}|, E)$ calculated by the optimization of all parameters B_i in the heuristic model of $\epsilon(\mathbf{Q})$ in the single mode approximation of $\tilde{S}(\mathbf{Q}, E)$ utilizing the refined values of $-n_{ij}J_{ij}\langle\hat{\mathbf{S}}_i \cdot \hat{\mathbf{S}}_j\rangle$ from the first moment sum rule. (c) Comparison of $|\mathbf{Q}|$ -integrated cuts ($|\mathbf{Q}|=[0,3] \text{\AA}^{-1}$) of measured and calculated $\tilde{S}_M(|\mathbf{Q}|, E)$. For the purposes of comparison, non-optimized $|\mathbf{Q}|$ -integrated cuts for all three types of dimensionality d are also presented. These cuts assume both $\epsilon(\mathbf{Q})$ possesses the same gap parameter B_o obtained from the 3D SMA fit in (b) and each permissible set of parameters is equally weighted. (d) Comparison of the measured and calculated $|\mathbf{Q}|$ -dependence of the first moment $\langle E \rangle$ integrated over E=[2,8] meV.

ferromagnetic coupling along a and b , respectively, while the larger positive l dispersion parameters correspond to stronger antiferromagnetic coupling along c , all consistent with both DC susceptibility and the refined magnetic structure presented in Fig. 2. The ability to describe the powder average magnetic dynamic response in terms of a coherent sharp mode is consistent with the cation order deduced from the critical scaling analysis and thus further evidence that the broadening of the magnetic excitations is due to powder averaging and not due to the underlying disorder.

IV. DISCUSSION

A. Experimental limitations

There are several limitations to the analysis presented in this paper. The first is the use of α -ZnV₃O₈ as a background for the analysis of the low temperature inelastic spectrum of α -CoV₃O₈. As shown in Fig. 1(d), α -ZnV₃O₈ crystallizes in the cation ordered $Iba2$ space group⁵³ and is thus not completely isostructural to α -CoV₃O₈. It can be argued that the local cation ordering deduced is an artefact of the $Iba2$ structure of the α -ZnV₃O₈ background. To counter such a claim, we point

out that the scaling analysis utilizing the same inelastic neutron scattering data, but after the subtraction of an independently calculated temperature-independent background derived from detailed balance^{123,124}, provided a critical exponent ν consistent with pure 3D Ising behavior. Such pure 3D Ising behavior would be unexpected if Co^{2+} was locally disordered.

Another limitation is the observation that the low temperature cooperative magnetism of $\alpha\text{-CoV}_3\text{O}_8$ can be treated as exclusively due to coupling between Co^{2+} moments. The presence of a second magnetic disordered “counter”-cation is in contrast to the model dilute 3D Ising antiferromagnets where the “counter”-cations are non-magnetic and thus interactions between magnetic ions of one type (e.g. Fe^{2+}) are exclusively considered^{6,13,47,48,159}. Such a situation was assumed to apply to $\alpha\text{-CoV}_3\text{O}_8$ in the analysis presented so far as a first approximation since there is evidence that V^{4+} behaves paramagnetically; but it is highly unlikely that coupling between V^{4+} and other V^{4+} or Co^{2+} plays no role in the low temperature magnetism and thus the analogy to the dilute antiferromagnets such as $\text{Fe}_x\text{Zn}_{1-x}\text{F}_2$ should be approached with caution. It is important to note that the apparent lack of influence of V^{4+} coupling, relative to coupling between Co^{2+} cations, may be due to the exclusive use of t_{2g} orbitals by V^{4+} , in contrast to the e_g orbitals utilized by Co^{2+} which is predicted to give much stronger coupling^{76-78,93,160}.

A further limitation concerns the nature of the competing ferromagnetic and antiferromagnetic interactions in $\alpha\text{-CoV}_3\text{O}_8$. In contrast to the $\text{Fe}_x\text{Zn}_{1-x}\text{F}_2$ series^{13,49,161}, $\alpha\text{-CoV}_3\text{O}_8$ exhibits both distinct ferromagnetic inter-chain and antiferromagnetic intra-chain coupling along the ab plane and along c , respectively. Both ferromagnetic and antiferromagnetic coupling possess similar magnitudes as proven by their near cancellation corresponding to a Weiss temperature near zero. With a Weiss temperature near zero, combined with a $T_N \sim 19$ K, the frustration index $f = \left| \frac{\theta_{CW}}{T_N} \right| \lesssim 1$ implies the absence of frustration, a key contributor to the rich phase diagram of the dilute 3D Ising antiferromagnets⁶. To address the concurrent presence of both ferromagnetic and antiferromagnetic couplings, it is worth noting that such a situation is reminiscent of another random dilute 3D Ising magnet system $\text{Fe}_x\text{Mg}_{1-x}\text{Cl}_2$ where $x > 0.55$, a series of compounds whose magnetic properties have been shown consistently to be qualitatively similar to that of $\text{Fe}_x\text{Zn}_{1-x}\text{F}_2$ ^{162,163}. To address the absence of frustration, it is worth noting that in contrast to the current study, previous work⁵² on smaller hydrothermally grown crystals of $\alpha\text{-CoV}_3\text{O}_8$ reported a $T_N = 8.2$ K and a Weiss temperature of -32.1 K, corresponding to a frustration index $f \sim 4$, indicating evidence for significant frustration. Such contrasting behavior provides strong evidence that sample dependence may play a significant role in determining the magnetic properties of $\alpha\text{-CoV}_3\text{O}_8$, as has been consistently observed for the dilute antiferromagnets, whose response functions are significantly influenced by both sample quality and non-equilibrium physics^{1,13,161}. The particular dependence on sample quality can be partially rationalized using recent work by Volkova¹⁶⁴ on $\alpha\text{-ZnV}_3\text{O}_8$. Numerical simulations indicated that although the ordered-*Iba2* arrangement was predicted to exhibit minimal frustration, if one

instead assumed a disordered-*Ibam* arrangement, significant magnetic frustration was predicted to manifest itself as competing inter-chain couplings of similar magnitudes in the presence of a dominant antiferromagnetic intra-chain coupling. The contrasting behavior between *Iba2* and *Ibam* cationic arrangement may provide an explanation for the aforementioned difference in the experimentally determined frustration indices with samples possessing more disorder exhibiting a larger value of f .

B. Disordered *Ibam* versus ordered *Iba2*?

A contradiction arises from a combined analysis of x-ray and neutron diffraction, DC susceptibility and inelastic neutron spectroscopy measurements in that the disordered-*Ibam* structure is derived from diffraction measurements, however the dynamics are more consistent with an ordered-*Iba2* arrangement of Co^{2+} ions. Diffraction indicates that statically the arrangement of Co^{2+} ions is disordered, however the collective long wavelength fluctuations seem to average out this disorder. $\alpha\text{-CoV}_3\text{O}_8$ therefore appears to be magnetically ordered for longer lengthscales. The disorder in $\alpha\text{-CoV}_3\text{O}_8$ differs from a Griffiths phase where local order is present and maybe more analogous to the situation in water ice where local selection rules are present.¹⁶⁵ However, the lack of strong diffuse scattering in our single crystal experiments makes a comparison to these correlated disordered systems difficult. However, the presence of the local selection structural selection for Co^{2+} and V^{4+} distinguishes CoV_3O_8 from a doped random magnet where no such local order is required. The apparent robustness of $\alpha\text{-CoV}_3\text{O}_8$ to disorder is discussed below in the context of spin-orbit coupling and comparison to other model magnets in a random field.

C. Universality class of $\alpha\text{-CoV}_3\text{O}_8$

Ising anisotropy is experimentally supported by several observations discussed above: the presence of a significant octahedral distortion ($\delta \sim 11$) as deduced from a combination of single crystal x-ray and neutron diffraction data, the presence of 3D Ising fluctuations as deduced from both critical exponents ν and β , and the presence of strong spin-orbit coupling supported by neutron spectroscopy. 3D dimensionality ($d = 3$) is suggested based on the following: the values of the critical exponents ν and β , the non-zero refined values of all h , k and l dispersion parameters in $\epsilon(\mathbf{Q})$ reflecting both strong coupling in both the ab plane and along c , in combination with the relatively weak anisotropy of the DC susceptibility.

The random magnetic cation distribution is supported by the refined *Ibam* structure from both single crystal x-ray and neutron diffraction and the value of β . An additional observation is the intrinsic width of the AFM transition as measured with DC susceptibility, reflected by the large experimental error of β caused by the rounding of the order parameter measurement, as has been experimentally observed in other dilute 3D Ising antiferromagnets such as $\text{Co}_x\text{Zn}_{1-x}\text{F}_2$ ¹⁶⁶. The dilution of 3D Ising magnetism can be rationalized by the key observation that V^{4+} appears to remain purely paramagnetic

down to 2 K and thus has no significant influence on the low temperature cooperative magnetic properties of α - CoV_3O_8 , as proven by a combination of inelastic neutron scattering and DC susceptibility measurements.

D. Comparison between α - CoV_3O_8 and Random Field Ising magnets

If one disregards the magnetic influence of V^{4+} , effectively treating the cation as a “counter”-ion such as Zn^{2+} in $\text{Fe}_x\text{Zn}_{1-x}\text{F}_2$ or $\text{Mn}_x\text{Zn}_{1-x}\text{F}_2$, then the magnetism due to Co^{2+} in α - CoV_3O_8 may be regarded as being magnetically diluted by 50%. Additionally, it is important to note that the failure to observe strong structural diffuse scattering with x-ray and neutron diffraction measurements is suggestive of a lack of local cation ordering or gradients. These concentration gradients were noted in dilute model antiferromagnets^{1,159,161,167–169}. Such a combination of significant dilution and disorder would be expected to have a significant effect on the dynamics^{1,11,12,20,49,51,116,170–172}. In this sense, it is surprising that there seems to be little effect on the magnetic dynamics in α - CoV_3O_8 , where the magnetic excitations are consistent with a fully ordered cation arrangement. Such behavior is suggestive that hydrodynamic and long wavelength fluctuations are not strongly sensitive to the disorder in α - CoV_3O_8 , in contrast with expectations based on theory^{173,174}. The robust nature of the dynamics to dilution, and in particular disorder is analogous to several observations in dilute random field magnets and in particular the $\text{Fe}_x\text{Zn}_{1-x}\text{F}_2$ series^{46,175,176}, where sharp excitations are still observable for large amount of doping⁴⁹. Unlike members of the $\text{Fe}_x\text{Zn}_{1-x}\text{F}_2$ series closer to the percolation threshold ($x_p \sim 0.24$) that exhibit spin glass behavior^{6,45,49,170}, $\text{Fe}_{0.5}\text{Zn}_{0.5}\text{F}_2$ assumes long range antiferromagnetic order in zero field with a T_N corresponding to half of that of FeF_2 ^{177,178}. The appearance of long range antiferromagnetic order as measured by DC susceptibility with a $\mu_o H_{ext} = 0.5$ T supports the claim that α - CoV_3O_8 is not close to the percolation threshold, where even the smallest external field destroys long range order, as is the case for $\text{M}_x\text{Zn}_{1-x}\text{F}_2$, where $\text{M} = \text{Co}^{2+}$ and Fe^{2+} ¹³¹. However, the random field Ising magnet $\text{Mn}_x\text{Zn}_{1-x}\text{F}_2$ ^{179,180} does show strong effects of the disorder on the dynamics. Such behavior is consistent with cases of random fields introduced through confinement where when the critical fluctuations have a similar length scale to the underlying disorder, the phase transition is strongly altered^{1,11,20,39,172}.

A key difference between MnF_2 and both α - CoV_3O_8 and FeF_2 is the presence of strong crystal field effects and spin-orbit coupling in the latter two compounds^{133,175}. It is also worth noting that unlike the case of pure CoO ^{81,91,94,181–184} where the large and far reaching exchange constants result in a significant and ultimately problematic entanglement of spin-orbit levels⁹⁴, in the case of α - CoV_3O_8 , the exchange constants are weak and the Weiss temperature is near 0 K. Both observations suggest that the presence of both strong crystal field effects and spin-orbit coupling with well-separated j_{eff} manifolds, as is the case for α - CoV_3O_8 , may be central to making the dynamics robust against strong disorder.

V. CONCLUDING REMARKS

In summary, a combination of zero field diffraction, DC susceptibility and neutron spectroscopy measurements have indicated that the low temperature cooperative magnetism of α - CoV_3O_8 is dominated by $j_{\text{eff}} = \frac{1}{2}$ Co^{2+} cations randomly distributed over the $16k$ metal site of the $Ibam$ structure, thus corresponding to an intrinsically disordered magnet without the need for any external influences such as chemical dopants or porous media. Despite the intrinsic disorder, by employing the sum rules of neutron scattering, the collective excitations have been shown to not be significantly affected by the disorder, displaying behavior consistent with an ordered- $Iba2$ arrangement of $j_{\text{eff}} = \frac{1}{2}$ Co^{2+} moments over a macroscopic scale. These Co^{2+} moments are coupled *via* a 3D network of competing ferromagnetic and stronger antiferromagnetic superexchange interactions within the ab plane and along c , respectively, resulting in long range antiferromagnetic order of the Co^{2+} moments at $T_N \sim 19$ K, despite a Weiss temperature near 0 K. A comparison of our results to the random 3D Ising magnets and other compounds where spin-orbit coupling is present indicate that both the presence of an orbital degree of freedom, in combination with strong crystal field effects and well-separated j_{eff} manifolds may be key in making the dynamics robust against disorder.

VI. ACKNOWLEDGEMENTS

We acknowledge discussions with J.A.M. Paddison, C.R. Wiebe, A.J. Browne, G. Perversi, S.E. Maytham (HBS) and D.R. Jarvis. We are grateful to the Royal Society, the STFC, the ERC and the EPSRC for financial support. P.M.S. acknowledges financial support from the CCSF, the RSC and the University of Edinburgh through the GRS and PCDS. We acknowledge the support of the National Institute of Standards and Technology, US Department of Commerce, in providing a portion of the neutron research facilities used in this work. Finally, the authors would like to thank the Carnegie Trust for the Universities of Scotland for providing facilities and equipment for chemical synthesis.

Appendix A: Crystallographic data

TABLE V. Crystal data, experimental and structural refinement parameters for single crystal x-ray diffraction measurements on α -CoV₃O₈. Numbers in parentheses indicate statistical errors.

Parameter	Value
Empirical Formula	CoV ₃ O ₈
Formula weight	339.7529 g mol ⁻¹
Temperature	120.0(1) K
Crystal Dimensions	0.40 × 0.11 × 0.09 mm ³
Wavelength	0.71073 Å (Mo K _α)
Crystal System	Orthorhombic
Space Group	<i>Ibam</i> (#72)
<i>a</i>	14.29344(4) Å
<i>b</i>	9.8740(3) Å
<i>c</i>	8.34000(3) Å
<i>V</i>	1185.60(6) Å ³
<i>Z</i>	8
ρ	3.8069(3) g cm ⁻³
θ range for data collection	4.13° ≤ θ ≤ 30.18°
Limiting Indices	-19 ≤ <i>h</i> ≤ 20, -13 ≤ <i>k</i> ≤ 14 and -11 ≤ <i>l</i> ≤ 11
Number of Reflections <i>I</i> > 0	985
Number of Reflections <i>I</i> > 3 σ (<i>I</i>)	910
Absorption Correction Method	Gaussian
Extinction Method	B-C Type 1 Gaussian Isotropic
Extinction Coefficient	2300(100)
Refinement Method	Full matrix least squares on <i>F</i> ²
Number of Parameters(Constraints)	67(9)
R _{F2} (<i>I</i> > 3 σ (<i>I</i>), all)	1.65%, 1.90%
R _{wF2} (<i>I</i> > 3 σ (<i>I</i>), all)	2.38%, 2.46%
Goodness-of-Fit χ^2 (<i>I</i> > 3 σ (<i>I</i>), all)	1.47%, 1.48%

TABLE VI. Structural parameters of α -CoV₃O₈ obtained from the refinement of single crystal x-ray diffraction data collected at 120 K. Numbers in parentheses indicate statistical errors.

Atom (Label)	Wyckoff Position	<i>x</i>	<i>y</i>	<i>z</i>	<i>B</i> _{iso} (Å ²)	Fractional Occupancy
Co	16 <i>k</i>	0.654760(16)	0.33285(2)	0.81060(3)	0.39(2)	0.506(6)
V(1)	16 <i>k</i>	0.654760(16)	0.33285(2)	0.81060(3)	0.39(2)	0.494(6)
V(2)	8 <i>j</i>	0.52271(2)	0.16672(4)	0.5	0.321(5)	1
V(3)	8 <i>j</i>	0.70168(2)	0.94348(4)	0.5	0.252(6)	1
O(1)	8 <i>j</i>	0.73349(11)	0.41325(16)	0	0.52(2)	1
O(2)	8 <i>j</i>	0.58248(10)	0.27500(16)	0	0.50(2)	1
O(3)	16 <i>k</i>	0.76787(8)	0.35258(11)	0.66386(15)	0.53(2)	1
O(4)	8 <i>f</i>	0.61080(11)	0.5	0.75	1.2(1)	1 ^a
O(5)	16 <i>k</i>	0.57900(8)	0.22361(12)	0.65802(16)	0.79(3)	1
O(6)	8 <i>j</i>	0.57973(10)	0.98272(16)	0.5	0.48(2)	1

^a The assignment of full occupancy in the 8*f* position corresponding to the bridging oxygen is in agreement with the initial refinement by Oka *et al.*⁵².

TABLE VII. Crystal data, experimental and structural refinement parameters for single crystal neutron diffraction measurements on α - CoV_3O_8 . Numbers in parentheses indicate statistical errors.

Parameter	Value
Empirical Formula	CoV_3O_8
Formula weight	$339.7529 \text{ g mol}^{-1}$
Temperature	$5.00(3) \text{ K}$
Crystal Dimensions	$13.2 \times 4.1 \times 2.1 \text{ mm}^3$
Wavelength	Polychromatic (time-of-flight)
Crystal System	Orthorhombic
Nuclear Space Group	$Ibam$ (#72)
Magnetic Space Group (BNS Setting)	$P1ccn$ (#56.376) or ($IPbam'$ OG 72.10.639)
\mathbf{k}	(111)
a	$14.3280(4) \text{ \AA}$
b	$9.9213(3) \text{ \AA}$
c	$8.4160(3) \text{ \AA}$
V	$1196.35(7) \text{ \AA}^3$
Z	8
ρ	$3.773(3) \text{ g cm}^{-3}$
θ range for data collection	$2.94^\circ \leq \theta \leq 76.22^\circ$
Limiting Indices	$-35 \leq h \leq 33, -25 \leq k \leq 19$ and $-16 \leq l \leq 22$
Number of Reflections $I > 0$	5120
Number of Reflections $I > 3\sigma(I)$	5086
Refinement Method	Full matrix least squares on F^2
Absorption Correction	None
Extinction Method	B-C Type 1 Gaussian Isotropic
Extinction Coefficient	$348(8)$
Number of Parameters(Constraints)	$34(10)$
μ_a	$1.35(4) \mu_B$
μ_b	$1.16(5) \mu_B$
μ_c	$3.05(4) \mu_B$
R_{F^2} ($I > 3\sigma(I)$, all)	8.34%, 8.38%
R_{wF^2} ($I > 3\sigma(I)$, all)	8.98%, 8.99%
$R_{F^2_{\text{mag}}}$ ($I > 3\sigma(I)$, all)	23.44%, 24.13%
Goodness-of-Fit χ^2 ($I > 3\sigma(I)$, all)	3.18, 3.19

TABLE VIII. Structural parameters for the nuclear structure of α - CoV_3O_8 obtained from the refinement of single crystal neutron diffraction data collected at 5 K. Numbers in parentheses indicate statistical errors.

Atom (Label)	Wyckoff Position	x	y	z	U_{iso} (\AA^2)	Fractional Occupancy ^a
Co	$16k$	$0.9068(3)$	$0.5765(3)$	$1.0616(5)$	$0.0005(5)$	$0.504(4)$
V(1)	$16k$	$0.9068(3)$	$0.5765(3)$	$1.0616(5)$	$0.0005(5)$	$0.496(4)$
V(2)	$8j$	0.771	0.416	0.75	0.0042	1
V(3)	$8j$	0.957	1.198	0.75	0.0042	1
O(1)	$8j$	$0.98357(9)$	$0.66282(11)$	0.25	$0.00356(16)$	1
O(2)	$8j$	$0.83242(8)$	$0.52523(11)$	0.25	$0.00388(16)$	1
O(3)	$16k$	$1.01787(6)$	$0.60246(8)$	$0.91384(10)$	$0.00392(11)$	1
O(4)	$8f$	$0.86076(9)$	0.75	1	$0.0126(4)$	1
O(5)	$16k$	$0.82899(6)$	$0.47373(8)$	$0.90801(10)$	$0.00556(12)$	1
O(6)	$8j$	$0.82973(8)$	$1.23252(10)$	0.75	$0.00269(15)$	1

^a The value of the fractional occupancies were fixed to the refined values obtained from a refinement of single crystal neutron diffraction data collected at 50 K.

TABLE IX. Cell parameters, fit residuals and agreement factors for α - CoV_3O_8 obtained from the Rietveld refinement of laboratory powder x-ray diffraction data collected at 300 K. Numbers in parentheses indicate statistical errors.

Parameter	Value
a	$14.292(1) \text{ \AA}$
b	$9.8844(9) \text{ \AA}$
c	$8.3969(8) \text{ \AA}$
V	$1186.2(3) \text{ \AA}^3$
χ^2	1.487
R_p	10.26%
R_{wp}	14.05%

TABLE X. Cobalt-oxygen distances and corresponding octahedral distortion parameter^{60,97} δ for α -CoV₃O₈ at 5 K deduced from the Rietveld refinement of single crystal neutron diffraction data. Numbers in parentheses indicate statistical errors.

Oxygen Label	d (Å)	$\left(\frac{d-\langle d \rangle}{\langle d \rangle}\right)^2 \times 10^4$
O(1)	2.12527(5)	27.79(3)
O(2)	1.98916(5)	2.162(8)
O(3)	2.07872(5)	8.79(2)
O(3)'	2.02358(5)	0.0549(13)
O(4)	1.92213(5)	22.95(3)
O(5)	1.97422(4)	4.89(1)
$\frac{1}{N} \sum \left\{ \left(\frac{d-\langle d \rangle}{\langle d \rangle}\right)^2 \times 10^4 \right\}$		11.106(8)

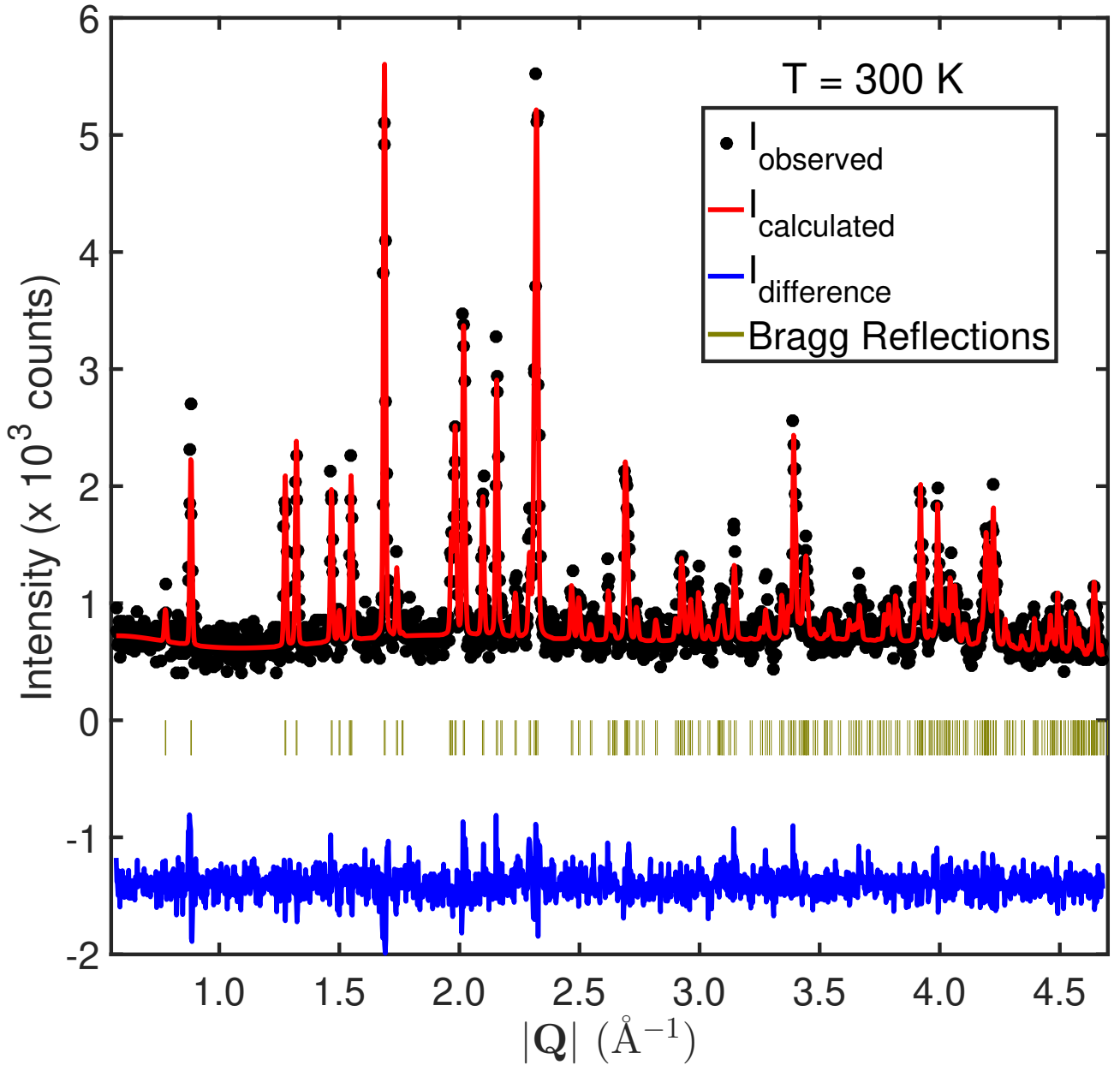


FIG. 9. Room temperature diffraction profile of polycrystalline α -CoV₃O₈ collected on a Bruker D2 Phaser x-ray diffractometer utilizing a monochromated Cu K $\alpha_{1,2}$ source, confirming the absence of any discernible impurities. A Rietveld refinement ($\chi^2 = 1.487$, $R_p = 10.26\%$, $R_{wp} = 14.05\%$) indicates α -CoV₃O₈ crystallizes in the orthorhombic $Ibam$ (S.G. #72) structure ($a = 14.292(1)$ Å, $b = 9.8844(9)$ Å, $c = 8.3969(8)$ Å).

Appendix B: Projection Factors

As outlined in the main text, a comparison between the current study and previous studies on other Co^{2+} -based magnets^{60,75,81,91,94,166,185} suggests that the low temperature magnetism of $\alpha\text{-CoV}_3\text{O}_8$ may be solely attributed to the ground state doublet spin-orbit manifold, and thus can be simplified to a $j = \frac{1}{2}$ model. To utilize such a model in the current study, the Landé g -factor g_J was required to be projected onto individual $j \equiv j_{\text{eff}}$ manifolds.

1. Calculation of the Orbital Angular Momentum Operator Projection Factor α

Before proceeding with the projection of the Landé g -factor onto the $j_{\text{eff}} = \frac{1}{2}$ ground state spin-orbit manifold, it is important to note that such a doublet manifold is a consequence of an approach commonly used^{60,75,81,91,94} to address the orbital triplet ground state in Co^{2+} . Such an approach first defines an effective total angular momentum $\hat{\mathbf{j}}_{\text{eff}} = \hat{\mathbf{I}} + \hat{\mathbf{S}}$, where $\hat{\mathbf{I}}$ is a fictitious orbital angular momentum operator, with eigenvalue $l=1$ to reflect an orbital triplet degeneracy¹⁰⁴. Thus, a projection of g_J and any angular momentum operators onto the $j = \frac{1}{2}$ manifold requires a concurrent projection of $\hat{\mathbf{L}}$ onto $\hat{\mathbf{I}}$, via a projection factor α .

The determination of the projection factor α begins by first defining the crystal field Hamiltonian $\hat{\mathcal{H}}_{CEF}$ describing the effects of the crystalline electric field on the free ion states of the d^7 Co^{2+} resulting from the symmetry imposed by the crystal lattice^{75,81,91,186}. Assuming both negligible distortions away from purely octahedral coordination and negligible admixture between the 4F ground and first excited 4P free ion states, a weak crystal field approach can be employed¹⁸⁷ whereby $\hat{\mathcal{H}}_{CEF}$ can be written in terms of the Stevens operators $\hat{\mathcal{O}}_4^0$, $\hat{\mathcal{O}}_4^4$ and the numerical coefficient B_4 as

$$\hat{\mathcal{H}}_{CEF} = B_4 \left(\hat{\mathcal{O}}_4^0 + 5\hat{\mathcal{O}}_4^4 \right). \quad (\text{B1})$$

The numerical coefficient B_4 is defined as $\beta\langle r^4 \rangle$ where β is the Stevens multiplicative factor, while the Stevens operators are defined in terms of the \hat{L}^2 , \hat{L}_z and \hat{L}_\pm orbital angular momentum operators^{104,187} as

$$\hat{\mathcal{O}}_4^0 = 35\hat{L}_z^4 - 30\hat{L}^2\hat{L}_z^2 + 25\hat{L}_z^2 - 6\hat{L}^2 + 3\hat{L}^4, \quad (\text{B2})$$

and

$$\hat{\mathcal{O}}_4^4 = \frac{1}{2} \left[\hat{L}_+^4 + \hat{L}_-^4 \right]. \quad (\text{B3})$$

By combining Eqs. B1-B3 and setting B_4 as -1 , the crystal field Hamiltonian is given by

$$\begin{bmatrix} -180 & 0 & 0 & 0 & -232.4 & 0 & 0 \\ 0 & 420 & 0 & 0 & 0 & -300 & 0 \\ 0 & 0 & -60 & 0 & 0 & 0 & -232.4 \\ 0 & 0 & 0 & -360 & 0 & 0 & 0 \\ -232.4 & 0 & 0 & 0 & -60 & 0 & 0 \\ 0 & -300 & 0 & 0 & 0 & 40 & 0 \\ 0 & 0 & -232.4 & 0 & 0 & 0 & -180 \end{bmatrix} \quad (\text{B4})$$

in the $|L=3, m_L\rangle$ basis where each operator has been normalized by \hbar . Before proceeding, it is worth noting that by setting $|B_4|$ as 1, all energy eigenstates will be in terms of B_4 while the negative sign is due to the d^7 electron configuration of Co^{2+} , producing a triplet and not a singlet ground state like Ni^{2+} ^{186,188}.

Diagonalizing the crystal field Hamiltonian yields

$$\begin{bmatrix} -360 & 0 & 0 & 0 & 0 & 0 & 0 \\ 0 & -360 & 0 & 0 & 0 & 0 & 0 \\ 0 & 0 & -360 & 0 & 0 & 0 & 0 \\ 0 & 0 & 0 & 120 & 0 & 0 & 0 \\ 0 & 0 & 0 & 0 & 120 & 0 & 0 \\ 0 & 0 & 0 & 0 & 0 & 120 & 0 \\ 0 & 0 & 0 & 0 & 0 & 0 & 720 \end{bmatrix} \quad (\text{B5})$$

corresponding to a triply degenerate ground state (Γ_4), a triply degenerate first excited state (Γ_5) and a singlet second excited state (Γ_2), where $\Delta(\Gamma_4 \rightarrow \Gamma_5) = 480B_4$ and $\Delta(\Gamma_5 \rightarrow \Gamma_2) = 600B_4$.

Utilizing the diagonalized crystal field Hamiltonian above, a transformation matrix \mathcal{C} can be defined as

$$\mathcal{C} = \begin{bmatrix} 0 & 0 & -0.79 & 0.61 & 0 & 0 & 0 \\ 0 & 0 & 0 & 0 & -0.71 & 0 & -0.71 \\ 0.61 & 0 & 0 & 0 & 0 & -0.79 & 0 \\ 0 & 1.00 & 0 & 0 & 0 & 0 & 0 \\ 0 & 0 & -0.61 & -0.79 & 0 & 0 & 0 \\ 0 & 0 & 0 & 0 & -0.71 & 0 & 0.71 \\ 0.79 & 0 & 0 & 0 & 0 & 0.61 & 0 \end{bmatrix} \quad (\text{B6})$$

where the columns of \mathcal{C} are the eigenvectors corresponding to the eigenvalues in Eq. B5. The eigenvectors are arranged in the order of increasing eigenvalues from left to right. In the case of degenerate eigenvalues, the eigenvectors are arranged in the order of increasing eigenvalues from left to right after the application of a small perturbative magnetic field $\hat{\mathcal{H}}_{MF} = H_{MF}\hat{S}_z$. The transformation matrix \mathcal{C} rotates operators from the $|L=3, m_L\rangle$ basis to a $|\phi_{CEF}\rangle$ basis defined by the crystal field eigenvectors by

$$\hat{\mathcal{O}}_{|\phi_{CEF}\rangle} = \mathcal{C}^{-1}\hat{\mathcal{O}}_{|L, m_L\rangle}\mathcal{C}. \quad (\text{B7})$$

Since the ground state multiplet of the crystal field Hamiltonian corresponds to the triply orbitally degenerate manifold, then the top 3×3 block matrix of the z -component of the orbital angular momentum operator projected onto the crystal field basis must¹⁶⁰: (1) have its matrix entries arranged in a format equivalent to its corresponding angular momentum operator with $l=1$, while (2) the entries in both matrices must be equal up to the projection constant α . Projecting the \hat{L}_z operator from the $|L=3, m_L\rangle$ basis to the $|\phi_{CEF}\rangle$ basis via Eq. B7, one obtains

$$\mathcal{C}^{-1}\hat{L}_z\mathcal{C} = \begin{bmatrix} 1.50 & 0 & 0 & 0 & 0 & -1.94 & 0 \\ 0 & 0 & 0 & 0 & 0 & 0 & 0 \\ 0 & 0 & -1.50 & -1.94 & 0 & 0 & 0 \\ 0 & 0 & -1.94 & -0.50 & 0 & 0 & 0 \\ 0 & 0 & 0 & 0 & 0 & 0 & 2.00 \\ -1.94 & 0 & 0 & 0 & 0 & 0.50 & 0 \\ 0 & 0 & 0 & 0 & 0 & 2.00 & 0 \end{bmatrix} \quad (\text{B8})$$

A comparison of the [top](#) and [middle](#) 3×3 block matrices in Eq. B8 to the \hat{L}_z operator (normalized by \hbar) in the $|l = 1, m_l\rangle$ basis given by

$$\hat{L}_z = \begin{bmatrix} -1 & 0 & 0 \\ 0 & 0 & 0 \\ 0 & 0 & 1 \end{bmatrix} \quad (\text{B9})$$

confirms that both block matrices have equivalent arrangements of matrix elements to \hat{L}_z operator in the $|l = 1, m_l\rangle$ basis, with projection factors $\alpha = -\frac{3}{2}$ and $\frac{1}{2}$ for the ground and first excited manifolds, respectively, in agreement with previous derivations utilizing group theory^{81,91,104,186}.

As a final confirmation of the validity of the projection described by Eq. B7, both \hat{L}_+ and \hat{L}_- were projected onto the $|\phi_{\text{CEF}}\rangle$ basis. Both \hat{L}_x and \hat{L}_y were then calculated using the following identities:

$$\hat{L}_x = \frac{\hat{L}_+ + \hat{L}_-}{2} \quad (\text{B10})$$

and

$$\hat{L}_y = \frac{\hat{L}_+ - \hat{L}_-}{2i}. \quad (\text{B11})$$

yielding:

$$\hat{L}_x = \left[\begin{array}{ccc|ccc|c} 0 & 1.1 & 0 & 0 & -1.4 & 0 & 0 \\ 1.1 & 0 & -1.1 & -1.4 & 0 & -1.4 & 0 \\ 0 & -1.1 & 0 & 0 & 1.4 & 0 & 0 \\ \hline 0 & -1.4 & 0 & 0 & 0.4 & 0 & -1.4 \\ -1.4 & 0 & 1.4 & 0.4 & 0 & 0.4 & 0 \\ 0 & -1.4 & 0 & 0 & 0.4 & 0 & 1.4 \\ \hline 0 & 0 & 0 & -1.4 & 0 & 1.4 & 0 \end{array} \right] \quad (\text{B12})$$

$$\hat{L}_y = i \left[\begin{array}{ccc|ccc|c} 0 & 1.1 & 0 & 0 & 0 & 0 & 0 \\ -1.1 & 0 & -1.1 & -1.4 & 0 & 1.4 & 0 \\ 0 & 1.1 & 0 & 0 & 1.4 & 0 & 0 \\ \hline 0 & 1.4 & 0 & 0 & 0.4 & 0 & -1.4 \\ -1.4 & 0 & -1.4 & -0.4 & 0 & 0.4 & 0 \\ 0 & -1.4 & 0 & 0 & -0.4 & 0 & -1.4 \\ \hline \xi & 0 & 0 & 1.4 & 0 & 1.4 & 0 \end{array} \right]. \quad (\text{B13})$$

Finally, by extracting the [top](#) 3×3 block matrices, denoted by a prime, from the definitions of \hat{L}_z (Eq. B8), \hat{L}_x (Eq. B12) and \hat{L}_y (Eq. B13) and evaluating the commutator $[\hat{L}'_x, \hat{L}'_y]$, one obtains

$$[\hat{L}'_x, \hat{L}'_y] = i \begin{bmatrix} 1.5 & 0 & 0 \\ 0 & 0 & 0 \\ 0 & 0 & -1.5 \end{bmatrix} = i\hat{L}'_z. \quad (\text{B14})$$

By performing the commutator of all possible permutations of the projected components of the orbital angular momentum operator, it can be shown that the canonical commutation relations of angular momentum¹⁰⁴, normalized by \hbar ,

$$[\hat{L}'_x, \hat{L}'_y] = i\epsilon_{xyz}\hat{L}'_z \quad (\text{B15})$$

are satisfied for the new $|\phi_{\text{CEF}}\rangle$ basis.

2. Calculation of Projected Landé g -Factor g'_J

Recall from first-order perturbation theory⁷⁵, the field splitting of the Co^{2+} spin-orbit multiplets is described by the perturbative Hamiltonian $\hat{\mathcal{H}}_m$ given by

$$\hat{\mathcal{H}}_m = \mu_B(g_L\hat{\mathbf{L}} + g_S\hat{\mathbf{S}}) \cdot \mathbf{H}, \quad (\text{B16})$$

where g_L and g_S denote orbital and spin g -factors, respectively. For the particular case of the d -block metal Co^{2+} , both orbital and spin g -factors are taken to be the electron's g -factors, equal to approximately 1 and 2, respectively, simplifying Eq. B16 to

$$\hat{\mathcal{H}}_m = \mu_B(\hat{\mathbf{L}} + 2\hat{\mathbf{S}}) \cdot \mathbf{H}. \quad (\text{B17})$$

Since an effective total angular momentum $\hat{\mathbf{j}}_{\text{eff}}$ was defined with the projected orbital angular momentum operator $\hat{\mathbf{L}}$ with $l = 1$, then the perturbative Hamiltonian in Eq. B17 becomes

$$\begin{aligned} \hat{\mathcal{H}}_m &= \mu_B(\alpha\hat{\mathbf{L}} + 2\hat{\mathbf{S}}) \cdot \mathbf{H} \\ &= g'_J\mu_B\hat{\mathbf{j}} \cdot \mathbf{H}, \end{aligned} \quad (\text{B18})$$

for a particular effective spin-orbit j_{eff} manifold. Eq. B18 incorporates an orbital angular momentum operator $\hat{\mathbf{L}}$ that has been projected onto $\hat{\mathbf{L}}$ *via* a projection factor α , and a projected Landé g -factor g'_J . A comparison between Eqs. B17 and B18 suggests that the Landé g -factor — a fundamental proportionality constant that can be derived directly from the Wigner-Eckart theorem⁹⁴ — defined as

$$\begin{aligned} g_J &= 1 \left\{ \frac{J(J+1) - S(S+1) + L(L+1)}{2J(J+1)} \right\} \\ &+ 2 \left\{ \frac{J(J+1) + S(S+1) - L(L+1)}{2J(J+1)} \right\} \end{aligned} \quad (\text{B19})$$

for the original non-projected perturbative Hamiltonian in Eq. B17 assumes the form

$$g'_J = \frac{(2 + \alpha)j(j+1) - (2 - \alpha)l(l+1) + (2 - \alpha)S(S+1)}{2j(j+1)}. \quad (\text{B20})$$

As required, Eq. B20 reduces to Eq. B19 if $\alpha = 1$. By inserting the values of $S = \frac{3}{2}$ to reflect the high spin d^7 electron configuration in ideal octahedral coordination, $l = 1$ to reflect the ground state crystal field manifold and the associated projection factor $\alpha = -\frac{3}{2}$, the projected Landé g -factor of $\frac{13}{3}$ is obtained for the $j_{\text{eff}} = \frac{1}{2}$ ground state spin-orbit manifold⁷⁵.

3. Calculation of Spin Angular Momentum Operator Projection Factor α'

As discussed in previous work^{75,81,91,94,166,185} on other systems whose magnetism is based on Co^{2+} in octahedral coordination, multiple projections of different angular momentum operators are necessary to consolidate

the measured low temperature magnetic excitations and the theoretical framework for a $j_{\text{eff}} = \frac{1}{2}$ ground state. One method¹⁶⁰ for such projections was presented in Appendix B1 and involved the use of linear transformations in the matrix representation of operators. Although powerful, this method relies on access to computation software and quickly becomes tedious as the dimension of the Hilbert space of interest increases. For the purposes of completion, we present an alternative method to project angular momentum operators onto a particular j_{eff} manifold. This method consists of a special case of the Wigner-Eckart theorem^{93,104}, called the projection theorem, given by

$$\hat{O} = \alpha' \hat{\mathbf{j}}_{\text{eff}} = \frac{\langle \hat{O} \cdot \hat{\mathbf{j}}_{\text{eff}} \rangle}{j(j+1)} \hat{\mathbf{j}}_{\text{eff}}, \quad (\text{B21})$$

describing the projection of an angular momentum operator \hat{O} onto an effective total angular momentum operator $\hat{\mathbf{j}}_{\text{eff}}$ via a projection factor α' . As introduced in Appendix B1, the operator $\hat{\mathbf{j}}_{\text{eff}} = \hat{\mathbf{l}} + \hat{\mathbf{S}}$ denotes an effective total angular momentum operator that utilizes a projection of an orbital angular momentum operator $\hat{\mathbf{L}}$ with $L = 3$ onto a fictitious orbital angular momentum operator $\hat{\mathbf{l}}$ with $l = 1$ via α .

For illustrative purposes, let \hat{O} be the spin angular momentum operator $\hat{\mathbf{S}}$. The numerator of the projection factor α' in Eq. B21 can be simplified by first using the distributive property of the inner product

$$\hat{\mathbf{S}} \cdot \hat{\mathbf{j}}_{\text{eff}} = \hat{\mathbf{S}} \cdot (\hat{\mathbf{l}} + \hat{\mathbf{S}}) = \hat{S}^2 + \hat{\mathbf{l}} \cdot \hat{\mathbf{S}}. \quad (\text{B22})$$

The inner product $\hat{\mathbf{l}} \cdot \hat{\mathbf{S}}$ on the RHS of Eq. B22 can be simplified to

$$\hat{\mathbf{l}} \cdot \hat{\mathbf{S}} = \frac{1}{2} \left[(\hat{j}_{\text{eff}})^2 - \hat{l}^2 - \hat{S}^2 \right], \quad (\text{B23})$$

since the inner product of $\hat{\mathbf{j}}_{\text{eff}}$ with itself is equal to

$$(\hat{j}_{\text{eff}})^2 = (\hat{\mathbf{l}} + \hat{\mathbf{S}}) \cdot (\hat{\mathbf{l}} + \hat{\mathbf{S}}) = \hat{l}^2 + \hat{S}^2 + 2\hat{\mathbf{l}} \cdot \hat{\mathbf{S}}. \quad (\text{B24})$$

Combining Eqs. B22 and B23, the numerator of α' in Eq. B21 becomes

$$\langle \hat{\mathbf{S}} \cdot \hat{\mathbf{j}}_{\text{eff}} \rangle = S(S+1) + \frac{1}{2} [j(j+1) - l(l+1) - S(S+1)], \quad (\text{B25})$$

where j_{eff} was relabeled as j . Inserting Eq. B25 into Eq. B21, one obtains

$$\hat{\mathbf{S}} = \frac{S(S+1) + \frac{1}{2} [j(j+1) - l(l+1) - S(S+1)]}{j(j+1)} \hat{\mathbf{j}}_{\text{eff}}, \quad (\text{B26})$$

which can be simplified algebraically to

$$\hat{\mathbf{S}} = \left\{ \frac{1}{2} + \frac{S(S+1) - l(l+1)}{2j(j+1)} \right\} \hat{\mathbf{j}}_{\text{eff}}. \quad (\text{B27})$$

Finally, by inserting the aforementioned values of $S = \frac{3}{2}$, $l = 1$ and $j \equiv j_{\text{eff}} = \frac{1}{2}$ for high spin Co^{2+} , Eq. B27 simplifies to

$$\hat{\mathbf{S}} = \frac{5}{3} \hat{\mathbf{j}}_{\text{eff}}. \quad (\text{B28})$$

A comparison between Eqs. B21 and B28 indicates that the projection factor α' of the spin orbital angular momentum operator is $\frac{5}{3}$ for the $j = \frac{1}{2}$ ground state spin-orbit manifold⁹⁴. It can be shown⁸¹ that one obtains the same value of α' employing the method outlined in Appendix B1 with the transformation matrix \mathcal{C} defined as the eigenvectors of the spin-orbit Hamiltonian $\hat{\mathcal{H}}_{SO} = \alpha \lambda \hat{\mathbf{l}} \cdot \hat{\mathbf{S}}$, where $\alpha = -\frac{3}{2}$ as derived in Appendix B1, $\lambda = -16$ meV as measured by Cowley *et al.*⁹¹, and $\hat{\mathbf{l}}$ is a fictitious orbital angular momentum operator with an eigenvalue $l=1$ as discussed above and in the main text.

Appendix C: Derivation of the Powder-Averaged First Moment Sum Rule of Neutron Scattering

The first moment sum rule of neutron scattering¹⁴⁵ states that

$$\langle E \rangle(\mathbf{Q}) = -\frac{2}{3} \sum_{i,j} n_{ij} J_{ij} \langle \hat{\mathbf{S}}_i \cdot \hat{\mathbf{S}}_j \rangle (1 - \cos(\mathbf{Q} \cdot \mathbf{d}_{ij})), \quad (\text{C1})$$

where J_{ij} , $n_{ij} \langle \hat{\mathbf{S}}_i \cdot \hat{\mathbf{S}}_j \rangle$, \mathbf{d}_{ij} denote the exchange constant, spin-spin correlator and displacement vector between spins i and j , respectively. Applying the definition of the powder average¹⁴⁶, Eq. C1 becomes

$$S(|\mathbf{Q}|, E) = \int d\Omega_{\hat{\mathbf{Q}}} \frac{S(\mathbf{Q}, E)}{4\pi}, \quad (\text{C2})$$

and utilizing the property of linearity of the integral, one obtains

$$- \frac{\mathcal{B}_{ij}}{12\pi} \int_0^\pi \int_0^{2\pi} (1 - \cos(|\mathbf{Q}||\mathbf{d}_{ij}| \cos \theta)) d\phi \sin \theta d\theta, \quad (\text{C3})$$

where \mathcal{B}_{ij} denotes $2n_{ij} J_{ij} \langle \hat{\mathbf{S}}_i \cdot \hat{\mathbf{S}}_j \rangle$ for a particular ij pair type. Using the substitution of $x = |\mathbf{Q}||\mathbf{d}_{ij}| \cos \theta$ in Eq. C3, one obtains

$$\frac{\mathcal{B}_{ij}}{3} \left(\frac{1}{4\pi} \right) \int_{|\mathbf{Q}||\mathbf{d}_{ij}|}^{-|\mathbf{Q}||\mathbf{d}_{ij}|} \int_0^{2\pi} (1 - \cos(x)) d\phi \frac{dx}{|\mathbf{Q}||\mathbf{d}_{ij}|}. \quad (\text{C4})$$

Employing the linearity property of the integral, the first term in Eq. C4 is reduced to

$$\frac{\mathcal{B}_{ij}}{3} \left(\frac{1}{4\pi} \right) \int_{|\mathbf{Q}||\mathbf{d}_{ij}|}^{-|\mathbf{Q}||\mathbf{d}_{ij}|} \int_0^{2\pi} \frac{d\phi dx}{|\mathbf{Q}||\mathbf{d}_{ij}|} = -\frac{\mathcal{B}_{ij}}{3}. \quad (\text{C5})$$

The second term in Eq. C4 becomes

$$- \frac{\mathcal{B}_{ij}}{3} \left(\frac{1}{4\pi} \right) \int_{|\mathbf{Q}||\mathbf{d}_{ij}|}^{-|\mathbf{Q}||\mathbf{d}_{ij}|} \int_0^{2\pi} \cos(x) \frac{d\phi dx}{|\mathbf{Q}||\mathbf{d}_{ij}|}, \quad (\text{C6})$$

which can be simplified by first integrating out $d\phi$,

$$-\frac{\mathcal{B}_{ij}}{3} \left(\frac{2\pi}{4\pi} \right) \int_{-|\mathbf{Q}||\mathbf{d}_{ij}|}^{|\mathbf{Q}||\mathbf{d}_{ij}|} \cos(x) \frac{dx}{|\mathbf{Q}||\mathbf{d}_{ij}|}, \quad (\text{C7})$$

which is equal to

$$-\frac{\mathcal{B}_{ij}}{3} \left(\frac{2\pi}{4\pi} \right) (\sin(-|\mathbf{Q}||\mathbf{d}_{ij}|) - \sin(|\mathbf{Q}||\mathbf{d}_{ij}|)). \quad (\text{C8})$$

Since sine is an odd function, Eq. C8 reduces to

$$\frac{\mathcal{B}_{ij}}{3} \left(\frac{\sin(|\mathbf{Q}||\mathbf{d}_{ij}|)}{|\mathbf{Q}||\mathbf{d}_{ij}|} \right). \quad (\text{C9})$$

Combining both terms, one obtains the final expression for the $|\mathbf{Q}|$ -dependence of the powder-averaged first moment as

$$\langle E \rangle(|\mathbf{Q}|) = -\frac{\mathcal{B}_{ij}}{3} \left(1 - \frac{\sin(|\mathbf{Q}||\mathbf{d}_{ij}|)}{|\mathbf{Q}||\mathbf{d}_{ij}|} \right). \quad (\text{C10})$$

The expression in Eq. C10 pertains to one particular ij pair-type. Utilizing the linearity property of the integral and replacing \mathcal{B}_{ij} by its definition, one can recover the sum from Eq. C1,

$$\langle E \rangle(\mathbf{Q}) = -\frac{2}{3} \sum_{i,j} n_{ij} J_{ij} \langle \hat{\mathbf{S}}_i \cdot \hat{\mathbf{S}}_j \rangle \left(1 - \frac{\sin(|\mathbf{Q}||\mathbf{d}_{ij}|)}{|\mathbf{Q}||\mathbf{d}_{ij}|} \right), \quad (\text{C11})$$

corresponding to Eq. 11 in the main text.

-
- ¹ D. S. Fisher and A. Khurana, *Phys. Today* **41**, 56 (1988).
² N. Martin, P. Bonville, E. Lhotel, S. Guitteny, A. Wildes, C. Decorse, M. Ciomaga-Hatnean, G. Balakrishnan, I. Mirebeau, and S. Petit, *Phys. Rev. X* **7**, 041028 (2017).
³ R. Sibille, E. Lhotel, M. C. Hatnean, G. J. Nilsen, G. Ehlers, A. Cervellino, E. Ressouche, M. Frontzek, O. Zaharko, V. Pomjakushin, *et al.*, *Nat. Commun.* **8**, 892 (2017).
⁴ S. F. Edwards and P. W. Anderson, *J. Phys. F: Met. Phys.* **5**, 965 (1975).
⁵ S. F. Edwards and P. W. Anderson, *J. Phys. F: Met. Phys.* **6**, 1927 (1976).
⁶ E. P. Raposo and M. D. Coutinho-Filho, *Phys. Rev. B* **57**, 3495 (1998).
⁷ O. Narayan and D. S. Fisher, *Phys. Rev. B* **42**, 7869 (1990).
⁸ L. Savary and L. Balents, *Phys. Rev. Lett.* **118**, 087203 (2017).
⁹ E. Altman, Y. Kafri, A. Polkovnikov, and G. Refael, *Phys. Rev. Lett.* **93**, 150402 (2004).
¹⁰ P. B. Weichman, *Mod. Phys. Lett. B* **22**, 2623 (2008).
¹¹ J. A. Hoyos and T. Vojta, *Phys. Rev. Lett.* **100**, 240601 (2008).
¹² T. Vojta, *Journal of Physics A: Mathematical and General* **39**, R143 (2006).
¹³ R. A. Cowley and W. J. L. Buyers, *Rev. Mod. Phys.* **44**, 406 (1972).
¹⁴ T. M. Nieuwenhuizen and C. N. A. van Duin, *Eur. Phys. J. B* **7**, 191 (1999).
¹⁵ L. Radzihovsky and J. Toner, *Phys. Rev. B* **60**, 206 (1999).
¹⁶ T. Bellini, L. Radzihovsky, J. Toner, and N. A. Clark, *Science* **294**, 1074 (2001).
¹⁷ J. Toner and D. P. DiVincenzo, *Phys. Rev. B* **41**, 632 (1990).
¹⁸ K. Binder and A. P. Young, *Rev. Mod. Phys.* **58**, 801 (1986).
¹⁹ H. Barghathi and T. Vojta, *Phys. Rev. Lett.* **109**, 170603 (2012).
²⁰ T. Vojta, "Computing quantum phase transitions," in *Reviews in Computational Chemistry* (Wiley-Blackwell, 2009) Chap. 4, pp. 167–221.
²¹ T. Giamarchi and P. Le Doussal, *Phys. Rev. B* **52**, 1242 (1995).
²² T. Klein, I. Joumard, S. Blanchard, J. Marcus, R. Cubitt, T. Giamarchi, and P. Le Doussal, *Nature* **413**, 404 (2001).
²³ A. D. Hernández and D. Domínguez, *Phys. Rev. Lett.* **92**, 117002 (2004).
²⁴ P. Olsson, *Phys. Rev. Lett.* **98**, 097001 (2007).
²⁵ D. Li and B. Rosenstein, *Phys. Rev. Lett.* **90**, 167004 (2003).
²⁶ M. J. P. Gingras and D. A. Huse, *Phys. Rev. B* **53**, 15193 (1996).
²⁷ D. S. Fisher, *Phys. Rev. Lett.* **78**, 1964 (1997).
²⁸ T. Giamarchi and P. Le Doussal, *Phys. Rev. Lett.* **72**, 1530 (1994).
²⁹ R. B. Griffiths, *Phys. Rev. Lett.* **23**, 17 (1969).
³⁰ A. J. Bray, *Phys. Rev. Lett.* **59**, 586 (1987).
³¹ B. M. McCoy, *Phys. Rev. Lett.* **23**, 383 (1969).
³² S. Park, R. L. Leheny, R. J. Birgeneau, J.-L. Gallani, C. W. Garland, and G. S. Iannacchione, *Phys. Rev. E* **65**, 050703 (2002).
³³ R. L. Leheny, S. Park, R. J. Birgeneau, J.-L. Gallani, C. W. Garland, and G. S. Iannacchione, *Phys. Rev. E* **67**, 011708 (2003).
³⁴ P. S. Clegg, C. Stock, R. J. Birgeneau, C. W. Garland, A. Rosh, and G. S. Iannacchione, *Phys. Rev. E* **67**, 021703 (2003).
³⁵ H. R. Glyde, *Reports on Progress in Physics* **81**, 014501 (2018).
³⁶ H. R. Glyde, O. Plantevin, B. Fåk, G. Coddens, P. S. Danielson, and H. Schober, *Phys. Rev. Lett.* **84**, 2646 (2000).
³⁷ J. V. Porto and J. M. Parpia, *Phys. Rev. Lett.* **74**, 4667 (1995).
³⁸ D. T. Sprague, T. M. Haard, J. B. Kycia, M. R. Rand, Y. Lee, P. J. Hamot, and W. P. Halperin, *Phys. Rev. Lett.* **75**, 661 (1995).
³⁹ M. Chan, N. Mulders, and J. Reppy, *Phys. Today* **49**, 30 (2018).
⁴⁰ Y. Imry and S.-k. Ma, *Phys. Rev. Lett.* **35**, 1399 (1975).
⁴¹ A. Aharony, Y. Imry, and S.-k. Ma, *Phys. Rev. Lett.* **37**, 1364 (1976).
⁴² S. M. A. Tabei, M. J. P. Gingras, Y.-J. Kao, P. Stasiak, and J.-Y. Fortin, *Phys. Rev. Lett.* **97**, 237203 (2006).
⁴³ D. Silevitch, D. Bitko, J. Brooke, S. Ghosh, G. Aeppli, and T. Rosenbaum, *Nature* **448**, 567 (2007).
⁴⁴ Z. Slanič, D. P. Belanger, and J. A. Fernandez-Baca, *Phys. Rev. Lett.* **82**, 426 (1999).
⁴⁵ G. Álvarez, N. Aso, D. P. Belanger, A. M. Durand, V. Martín-Mayor, K. Motoya, and Y. Muro, *Phys. Rev. B* **86**, 024416 (2012).
⁴⁶ Y. W. Rodriguez, I. E. Anderson, D. P. Belanger, H. Nojiri, F. Ye, and J. A. Fernandez-Baca, *J. Magn. Magn. Mater.* **310**, 1546 (2007), proceedings of the 17th Inter-

- national Conference on Magnetism.
- ⁴⁷ R. A. Cowley, H. Yoshizawa, G. Shirane, and R. J. Birgeneau, *Z Phys. B Con. Mat.* **58**, 15 (1984).
- ⁴⁸ R. J. Birgeneau and Y. J. Uemura, *Journal of Applied Physics* **61**, 3692 (1987).
- ⁴⁹ C. Paduani, D. P. Belanger, J. Wang, S.-J. Han, and R. M. Nicklow, *Phys. Rev. B* **50**, 193 (1994).
- ⁵⁰ R. Leheny, Y. Lee, G. Shirane, and R. Birgeneau, *Eur. Phys. J. B* **32**, 287 (2003).
- ⁵¹ T. Vojta, *AIP Conf. Proc.* **1550**, 188 (2013).
- ⁵² Y. Oka, T. Yao, N. Yamamoto, and Y. Ueda, *J. Solid State Chem.* **141**, 133 (1998).
- ⁵³ D. J. Lloyd and J. Galy, *Cryst. Struct. Commun.* **2**, 209 (1973).
- ⁵⁴ S. Fishman and A. Aharony, *J. Phys. C: Solid State Phys.* **12**, L729 (1979).
- ⁵⁵ P. W. Anderson, *Phys. Rev.* **109**, 1492 (1958).
- ⁵⁶ A. Croy, P. Cain, and M. Schreiber, *Eur. Phys. J. C* **82**, 107 (2011).
- ⁵⁷ F. A. B. F. de Moura and M. L. Lyra, *Phys. Rev. Lett.* **81**, 3735 (1998).
- ⁵⁸ Z. He, J.-I. Yamaura, Y. Ueda, and W. Cheng, *J. Am. Chem. Soc.* **131**, 7554 (2009).
- ⁵⁹ M. Markkula, A. M. Arévalo-López, and J. P. Attfield, *J. Solid State Chem.* **192**, 390 (2012).
- ⁶⁰ F. Wallington, A. M. Arévalo-López, J. W. Taylor, J. R. Stewart, V. García-Sakai, J. P. Attfield, and C. Stock, *Phys. Rev. B* **92**, 125116 (2015).
- ⁶¹ S. Ichikawa, M. Hibino, and T. Yao, *Asian J. Energy Environ.* **8**, 33 (2007).
- ⁶² Agilent-CrysAlisPRO, Yarnton, Oxfordshire, England (2013).
- ⁶³ O. V. Dolomanov, L. J. Bourhis, R. J. Gildea, J. A. Howard, and H. Puschmann, *J. Appl. Crystallogr.* **42**, 339 (2009).
- ⁶⁴ V. Petříček, M. Dušek, and L. Palatinus, *Z. Kristallogr. Cryst. Mater.* **229**, 345 (2014).
- ⁶⁵ B. H. Toby, *J. Appl. Crystallogr.* **34**, 210 (2001).
- ⁶⁶ W. Whitley, C. Stock, and A. D. Huxley, *J. Appl. Crystallogr.* **48**, 1342 (2015).
- ⁶⁷ C. L. Bull, M. W. Johnson, H. Hamidov, K. Komatsu, M. Guthrie, M. J. Gutmann, J. S. Loveday, and R. J. Nelmes, *J. Appl. Crystallogr.* **47**, 974 (2014).
- ⁶⁸ M. J. Gutmann, V. Petříček, M. A. Daoud-Aladine, and C. Y. Martin, *Meas. Sci. Technol.* **19**, 034005 (2008).
- ⁶⁹ M. Gutmann, *Acta Cryst. A* **61**, c164 (2005).
- ⁷⁰ C. Stock, R. A. Cowley, J. W. Taylor, and S. M. Bennington, *Phys. Rev. B* **81**, 024303 (2010).
- ⁷¹ K. H. Andersen, *Nucl. Instr. Meth. Phys. Res. A* **371**, 472 (1996).
- ⁷² F. Hippert, E. Geissler, J. L. Hodeau, E. Lelièvre-Berna, and J.-R. Regnard, *Neutron and X-ray Spectroscopy* (Springer Science & Business Media, Berlin, 2006).
- ⁷³ C. J. Carlile, M. A. Adams, P. S. R. Krishna, M. Prager, K. Shibata, and P. Westerhuijs, *Nucl. Instr. Meth. Phys. Res. A* **338**, 78 (1994).
- ⁷⁴ National Institute of Standards and Technology, *NIST Center for Neutron Research Accomplishments and Opportunities*, ASTM Special Technical Publication, Vol. 962 (Department of Commerce, United States of America, 2001).
- ⁷⁵ W. Buyers, T. Holden, E. Svensson, R. Cowley, and M. Hutchings, *J. Phys. C* **4**, 2139 (1971).
- ⁷⁶ J. B. Goodenough, *Phys. Rev.* **100**, 564 (1955).
- ⁷⁷ J. B. Goodenough, *J. Phys. Chem. Solids* **6**, 287 (1958).
- ⁷⁸ J. Kanamori, *J. Phys. Chem. Solids* **10**, 87 (1959).
- ⁷⁹ Z. Ropka and R. J. Radwanski, *Czech J Phys* **54**, 427 (2004).
- ⁸⁰ J. L. Gavilano, D. Rau, S. Mushkolaj, H. R. Ott, P. Millet, and F. Mila, *Phys. Rev. Lett.* **90**, 167202 (2003).
- ⁸¹ J. Kanamori, *Progr. Theor. Exp. Phys.* **17**, 177 (1957).
- ⁸² B. Kim, B. H. Kim, K. Kim, H. C. Choi, S.-Y. Park, Y. H. Jeong, and B. I. Min, *Phys. Rev. B* **85**, 220407 (2012).
- ⁸³ D. B. Litvin, *Magnetic Group Tables: 1-, 2- and 3-Dimensional Magnetic Subperiodic Groups and Magnetic Space Groups* (IUCR, 2013).
- ⁸⁴ M. De Graef, *Metall. Mater. Trans. A* **41**, 1321 (2010).
- ⁸⁵ G. Xu, Z. Xu, and J. Tranquada, *Rev. Sci. Instrum.* **84**, 083906 (2013).
- ⁸⁶ Z. Xu, J. Wen, T. Berlijn, P. M. Gehring, C. Stock, M. B. Stone, W. Ku, G. Gu, S. M. Shapiro, R. J. Birgeneau, and G. Xu, *Phys. Rev. B* **86**, 174419 (2012).
- ⁸⁷ C. Stock, L. C. Chapon, O. Adamopoulos, A. Lappas, M. Giot, J. W. Taylor, M. A. Green, C. M. Brown, and P. G. Radaelli, *Phys. Rev. Lett.* **103**, 077202 (2009).
- ⁸⁸ H. F. Fong, P. Bourges, Y. Sidis, L. P. Regnault, J. Bossy, A. Ivanov, D. L. Milius, I. A. Aksay, and B. Keimer, *Phys. Rev. B* **61**, 14773 (2000).
- ⁸⁹ G. L. Squires, *Introduction to the Theory of Thermal Neutron Scattering*, 3rd ed. (Cambridge University Press, 2012).
- ⁹⁰ C. Stock, W. J. L. Buyers, R. Liang, D. Peets, Z. Tun, D. Bonn, W. N. Hardy, and R. J. Birgeneau, *Phys. Rev. B* **69**, 014502 (2004).
- ⁹¹ R. A. Cowley, W. J. L. Buyers, C. Stock, Z. Yamani, C. Frost, J. W. Taylor, and D. Prabhakaran, *Phys. Rev. B* **88**, 205117 (2013).
- ⁹² W. J. L. Buyers, R. A. Cowley, T. M. Holden, and R. W. H. Stevenson, *J. Appl. Phys.* **39**, 1118 (1968).
- ⁹³ D. I. Khomskii, *Transition Metal Compounds* (Cambridge University Press, 2014).
- ⁹⁴ P. M. Sarte, R. A. Cowley, E. E. Rodriguez, E. Pachoud, D. Le, V. García-Sakai, J. W. Taylor, C. D. Frost, D. Prabhakaran, C. MacEwen, A. Kitada, A. J. Browne, M. Songvilay, Z. Yamani, W. J. L. Buyers, J. P. Attfield, and C. Stock, *Phys. Rev. B* **98**, 024415 (2018).
- ⁹⁵ R. A. Cowley, W. J. L. Buyers, P. Martel, and R. W. H. Stevenson, *J. Phys. C: Solid State Phys.* **6**, 2997 (1973).
- ⁹⁶ P. Martel, R. A. Cowley, and R. W. H. Stevenson, *Canadian Journal of Physics* **46**, 1355 (1968).
- ⁹⁷ A. M. Abakumov, R. Erni, A. A. Tsirlin, M. D. Rossell, D. Batuk, G. Nenert, and G. V. Tendeloo, *Chemistry of Materials* **25**, 2670 (2013).
- ⁹⁸ H. M. Gladney, *Phys. Rev.* **146**, 253 (1966).
- ⁹⁹ U. Walter, *J. Phys. Chem. Solids* **45**, 401 (1984).
- ¹⁰⁰ M. B. Stone, I. Zaliznyak, D. H. Reich, and C. Broholm, *Phys. Rev. B* **64**, 144405 (2001).
- ¹⁰¹ J. Lorenzana, G. Seibold, and R. Coldea, *Phys. Rev. B* **72**, 224511 (2005).
- ¹⁰² K. W. Plumb, J. R. Morey, J. A. Rodriguez-Rivera, H. Wu, A. A. Podlesnyak, T. M. McQueen, and C. L. Broholm, *Phys. Rev. X* **6**, 041055 (2016).
- ¹⁰³ P. R. Hammar, D. H. Reich, C. Broholm, and F. Trouw, *Phys. Rev. B* **57**, 7846 (1998).
- ¹⁰⁴ A. Abragam and B. Bleaney, *Electron Paramagnetic Resonance of Transition Ions* (Dover Publications, New York, 1986).
- ¹⁰⁵ T. Holden, W. Buyers, E. Svensson, R. Cowley, M. Hutchings, D. Hukin, and R. Stevenson, *J. Phys. C* **4**, 2127 (1971).
- ¹⁰⁶ C. Stock, C. Broholm, F. Demmel, J. Van Duijn, J. W. Taylor, H. J. Kang, R. Hu, and C. Petrovic, *Phys. Rev. Lett.* **109**, 127201 (2012).
- ¹⁰⁷ S. A. J. Kimber, H. Mutka, T. Chatterji, T. Hofmann, P. F. Henry, H. N. Bordallo, D. N. Argyriou, and J. P. Attfield, *Phys. Rev. B* **84**, 104425 (2011).
- ¹⁰⁸ R. Radwanski and Z. Ropka, *Physica B Condens. Matter* **345**, 107 (2004), proceedings of the Conference on Polarised Neutron and Synchrotron X-rays for Magnetism.
- ¹⁰⁹ W. Neubeck, C. Vettier, F. de Bergevin, F. Yakhov, D. Mannix, L. Ranno, and T. Chatterji, *J. Phys. Chem.*

- Solids **62**, 2173 (2001).
- ¹¹⁰ R. Birgeneau, A. Aharony, N. Belk, F. Chou, Y. Endoh, M. Greven, S. Hosoya, M. Kastner, C. Lee, Y. Lee, G. Shirane, S. Wakimoto, B. Wells, and K. Yamada, *J. Phys. Chem. Solids* **56**, 1913 (1995).
- ¹¹¹ M. Greven, R. J. Birgeneau, Y. Endoh, M. A. Kastner, M. Matsuda, and G. Shirane, *Z Phys B Con Mat* **96**, 465 (1995).
- ¹¹² M. Songvilay, S. Petit, V. Hardy, J. P. Castellan, G. André, C. Martin, and F. Damay, *Phys. Rev. B* **91**, 054408 (2015).
- ¹¹³ J. van Duijn, K. H. Kim, N. Hur, D. Adroja, M. A. Adams, Q. Z. Huang, M. Jaime, S.-W. Cheong, C. Broholm, and T. G. Perring, *Phys. Rev. Lett.* **94**, 177201 (2005).
- ¹¹⁴ B. D. Gaulin, E. Kermarrec, M. L. Dahlberg, M. J. Matthews, F. Bert, J. Zhang, P. Mendels, K. Fritsch, G. E. Granroth, P. Jiramongkolchai, A. Amato, C. Baines, R. J. Cava, and P. Schiffer, *Phys. Rev. B* **91**, 245141 (2015).
- ¹¹⁵ J. Gaudet, D. D. Maharaj, G. Sala, E. Kermarrec, K. A. Ross, H. A. Dabkowska, A. I. Kolesnikov, G. E. Granroth, and B. D. Gaulin, *Phys. Rev. B* **92**, 134420 (2015).
- ¹¹⁶ Y. J. Uemura and R. J. Birgeneau, *Phys. Rev. B* **36**, 7024 (1987).
- ¹¹⁷ C. Stock, W. J. L. Buyers, Z. Yamani, Z. Tun, R. J. Birgeneau, R. Liang, D. Bonn, and W. N. Hardy, *Phys. Rev. B* **77**, 104513 (2008).
- ¹¹⁸ R. J. Birgeneau, R. W. Erwin, P. M. Gehring, M. A. Kastner, B. Keimer, M. Sato, S. Shamoto, G. Shirane, and J. Tranquada, *Z. Phys. B Con. Mat.* **87**, 15 (1992).
- ¹¹⁹ W. Bao, Y. Chen, Y. Qiu, and J. L. Sarrao, *Phys. Rev. Lett.* **91**, 127005 (2003).
- ¹²⁰ B. Keimer, R. J. Birgeneau, A. Cassanho, Y. Endoh, R. W. Erwin, M. A. Kastner, and G. Shirane, *Phys. Rev. Lett.* **67**, 1930 (1991).
- ¹²¹ S. D. Wilson, S. Li, P. Dai, W. Bao, J.-H. Chung, H. J. Kang, S.-H. Lee, S. Komiyama, Y. Ando, and Q. Si, *Phys. Rev. B* **74**, 144514 (2006).
- ¹²² M. Collins, *Magnetic Critical Scattering*, Oxford series on neutron scattering in condensed matter (Oxford University Press, 1989).
- ¹²³ C. Stock, E. E. Rodriguez, and M. A. Green, *Phys. Rev. B* **85**, 094507 (2012).
- ¹²⁴ T. Hong, M. Kenzelmann, M. M. Turnbull, C. P. Landee, B. D. Lewis, K. P. Schmidt, G. S. Uhrig, Y. Qiu, C. Broholm, and D. Reich, *Phys. Rev. B* **74**, 094434 (2006).
- ¹²⁵ T. Mason, in *High-Temperature Superconductors - II*, Handbook on the Physics and Chemistry of Rare Earths, Vol. 31 (Elsevier, 2001) pp. 281 – 314.
- ¹²⁶ A. Schröder, G. Aeppli, R. Coldea, M. Adams, O. Stockert, H. Löhneysen, E. Bucher, R. Ramazashvili, and P. Coleman, *Nature* **407**, 351 (2000).
- ¹²⁷ O. Stockert, M. Enderle, and H. v. Löhneysen, *Phys. Rev. Lett.* **99**, 237203 (2007).
- ¹²⁸ A. J. Millis, *Phys. Rev. B* **48**, 7183 (1993).
- ¹²⁹ J. D. Jackson, *Classical electrodynamics*, 3rd ed. (Wiley, New York, NY, 1999).
- ¹³⁰ B. L. Bean and J. R. Izatt, *J. Opt. Soc. Am.* **63**, 832 (1973).
- ¹³¹ M. Hagen, R. A. Cowley, S. K. Satija, H. Yoshizawa, G. Shirane, R. J. Birgeneau, and H. J. Guggenheim, *Phys. Rev. B* **28**, 2602 (1983).
- ¹³² W. Bao, C. Broholm, G. Aeppli, S. A. Carter, P. Dai, T. F. Rosenbaum, J. M. Honig, P. Metcalf, and S. F. Trevino, *Phys. Rev. B* **58**, 12727 (1998).
- ¹³³ M. T. Hutchings, M. P. Schulhof, and H. J. Guggenheim, *Phys. Rev. B* **5**, 154 (1972).
- ¹³⁴ M. F. Collins, V. J. Minkiewicz, R. Nathans, L. Passell, and G. Shirane, *Phys. Rev.* **179**, 417 (1969).
- ¹³⁵ M. P. Schulhof, R. Nathans, P. Heller, and A. Linz, *Phys. Rev. B* **4**, 2254 (1971).
- ¹³⁶ H. Chou, J. M. Tranquada, G. Shirane, T. E. Mason, W. J. L. Buyers, S. Shamoto, and M. Sato, *Phys. Rev. B* **43**, 5554 (1991).
- ¹³⁷ Q. Si, S. Rabello, K. Ingersent, and J. L. Smith, *Nature* **413**, 804 (2001).
- ¹³⁸ M. Hasenbusch, F. P. Toldin, A. Pelissetto, and E. Vicari, *J. Stat. Mech.* **2007**, P02016 (2007).
- ¹³⁹ H. G. Ballesteros, L. A. Fernández, V. Martín-Mayor, A. Muñoz Sudupe, G. Parisi, and J. J. Ruiz-Lorenzo, *Phys. Rev. B* **58**, 2740 (1998).
- ¹⁴⁰ P. Calabrese, V. Martín-Mayor, A. Pelissetto, and E. Vicari, *Phys. Rev. E* **68**, 036136 (2003).
- ¹⁴¹ P. Calabrese, A. Pelissetto, and E. Vicari, *Phys. Rev. B* **68**, 092409 (2003).
- ¹⁴² M. J. George and J. J. Rehr, *Phys. Rev. Lett.* **53**, 2063 (1984).
- ¹⁴³ C. Stock, L. C. Chapon, A. Schneidewind, Y. Su, P. G. Radaelli, D. F. McMorrow, A. Bombardi, N. Lee, and S.-W. Cheong, *Phys. Rev. B* **83**, 104426 (2011).
- ¹⁴⁴ S. D. Wilson, Z. Yamani, C. R. Rotundu, B. Freelon, E. Bourret-Courchesne, and R. J. Birgeneau, *Phys. Rev. B* **79**, 184519 (2009).
- ¹⁴⁵ P. C. Hohenberg and W. F. Brinkman, *Phys. Rev. B* **10**, 128 (1974).
- ¹⁴⁶ J. T. Haraldsen, T. Barnes, and J. L. Musfeldt, *Phys. Rev. B* **71**, 064403 (2005).
- ¹⁴⁷ G. Xu, C. Broholm, D. H. Reich, and M. A. Adams, *Phys. Rev. Lett.* **84**, 4465 (2000).
- ¹⁴⁸ E. E. McCabe, C. Stock, E. E. Rodriguez, A. S. Wills, J. W. Taylor, and J. S. O. Evans, *Phys. Rev. B* **89**, 100402 (2014).
- ¹⁴⁹ S. Ma, C. Broholm, D. H. Reich, B. J. Sternlieb, and R. W. Erwin, *Phys. Rev. Lett.* **69**, 3571 (1992).
- ¹⁵⁰ S. M. Girvin, A. H. MacDonald, and P. M. Platzman, *Phys. Rev. B* **33**, 2481 (1986).
- ¹⁵¹ E. C. Svensson, W. J. L. Buyers, T. M. Holden, R. A. Cowley, and R. W. Stevenson, *Can. J. Phys.* **47**, 1983 (1969).
- ¹⁵² M. Ramazanoglu, C. P. Adams, J. P. Clancy, A. J. Berlinsky, Z. Yamani, R. Szymczak, H. Szymczak, J. Fink-Finowicki, and B. D. Gaulin, *Phys. Rev. B* **79**, 024417 (2009).
- ¹⁵³ K. Lee, J. Lee, C. Lee, and M. Whangbo, *Bull. Korean Chem. Soc.* **35**, 1277 (2014).
- ¹⁵⁴ C. Kittel, *Introduction to solid state physics* (Wiley, New York, 2005).
- ¹⁵⁵ M. B. Stone, Y. Chen, J. Rittner, H. Yardimci, D. H. Reich, C. Broholm, D. V. Ferraris, and T. Lectka, *Phys. Rev. B* **65**, 064423 (2002).
- ¹⁵⁶ R. J. Birgeneau, Q. Feng, Q. J. Harris, J. P. Hill, A. P. Ramirez, and T. R. Thurston, *Phys. Rev. Lett.* **75**, 1198 (1995).
- ¹⁵⁷ Y. J. Kim, R. J. Birgeneau, F. C. Chou, M. Greven, M. A. Kastner, Y. S. Lee, B. O. Wells, A. Aharony, O. Entin-Wohlman, I. Y. Korenblit, A. B. Harris, R. W. Erwin, and G. Shirane, *Phys. Rev. B* **64**, 024435 (2001).
- ¹⁵⁸ I. Cabrera, J. D. Thompson, R. Coldea, D. Prabhakaran, R. I. Bewley, T. Guidi, J. A. Rodriguez-Rivera, and C. Stock, *Phys. Rev. B* **90**, 014418 (2014).
- ¹⁵⁹ A. P. Young, *Spin Glasses and Random Fields*, Directions in condensed matter physics (World Scientific, 1998).
- ¹⁶⁰ G. L. Stamokostas and G. A. Fiete, *Phys. Rev. B* **97**, 085150 (2018).
- ¹⁶¹ A. R. King and V. Jaccarino, *J. Appl. Phys.* **52**, 1785 (1981).
- ¹⁶² J. Mattsson, J. Kushauer, D. Bertrand, J. Ferr, and W. Kleemann, *J. Magn. Magn. Mater.* **130**, 216 (1994).
- ¹⁶³ N. G. Fytas, V. Martín-Mayor, M. Picco, and N. Sourlas, *J. Stat. Phys.* (2018), 10.1007/s10955-018-1955-7.
- ¹⁶⁴ L. M. Volkova, *J. Phys. Condens. Matter* **19**, 176208 (2007).
- ¹⁶⁵ D. A. Keen and A. L. Goodwin, *Nature* **521**, 303 (2015).

- ¹⁶⁶ R. S. Cowley and K. Carneiro, *J. Phys. C: Solid State Phys.* **13**, 3281 (1980).
- ¹⁶⁷ G. D'Ariano and F. Borsa, *Phys. Rev. B* **26**, 6215 (1982).
- ¹⁶⁸ C. A. Ramos, A. R. King, and V. Jaccarino, *Phys. Rev. B* **37**, 5483 (1988).
- ¹⁶⁹ D. P. Belanger, A. R. King, I. B. Ferreira, and V. Jaccarino, *Phys. Rev. B* **37**, 226 (1988).
- ¹⁷⁰ D. P. Belanger and H. Yoshizawa, *Phys. Rev. B* **47**, 5051 (1993).
- ¹⁷¹ T. Terao, K. Yakubo, and T. Nakayama, *Phys. Rev. E* **50**, 566.
- ¹⁷² M. Vojta, *Phys. Rev. Lett.* **111**, 097202 (2013).
- ¹⁷³ I. Y. Korenblit and E. F. Shender, *Phys. Rev. B* **48**, 9478 (1993).
- ¹⁷⁴ C. C. Wan, A. B. Harris, and D. Kumar, *Phys. Rev. B* **48**, 1036 (1993).
- ¹⁷⁵ M. Hutchings, B. Rainford, and H. Guggenheim, *J. Phys. C: Solid State Phys.* **3**, 307 (1970).
- ¹⁷⁶ C. B. de Araujo, *Phys. Rev. B* **22**, 266 (1980).
- ¹⁷⁷ R. J. Birgeneau, R. A. Cowley, G. Shirane, H. Yoshizawa, D. P. Belanger, A. R. King, and V. Jaccarino, *Phys. Rev. B* **27**, 6747 (1983).
- ¹⁷⁸ J. P. Hill, Q. Feng, Q. J. Harris, R. J. Birgeneau, A. P. Ramirez, and A. Cassanho, *Phys. Rev. B* **55**, 356 (1997).
- ¹⁷⁹ P. W. Mitchell, R. A. Cowley, H. Yoshizawa, P. Böni, Y. J. Uemura, and R. J. Birgeneau, *Phys. Rev. B* **34**, 4719 (1986).
- ¹⁸⁰ G. J. Coombs, R. A. Cowley, W. J. L. Buyers, E. C. Svensson, T. M. Holden, and D. A. Jones, *J. Phys. C: Solid State Phys.* **9**, 2167 (1976).
- ¹⁸¹ Z. Yamani, W. J. L. Buyers, R. A. Cowley, and D. Prabhakaran, *Physica B* **403**, 1406 (2008).
- ¹⁸² T. Satoh, R. Iida, T. Higuchi, Y. Fujii, A. Koreeda, H. Ueda, T. Shimura, K. Kuroda, V. I. Butrim, and B. A. Ivanov, *Nat. Commun.* **8**, 638 (2017).
- ¹⁸³ K. Tomiyasu and S. Itoh, *J. Phys. Soc. Jpn* **75**, 084708 (2006).
- ¹⁸⁴ M. Feyngenson, X. Teng, S. E. Inderhees, Y. Yiu, W. Du, W. Han, J. Wen, Z. Xu, A. A. Podlesnyak, J. L. Niedziela, M. Hagen, Y. Qiu, C. M. Brown, L. Zhang, and M. C. Aronson, *Phys. Rev. B* **83**, 174414 (2011).
- ¹⁸⁵ K. A. Ross, J. W. Krizan, J. A. Rodriguez-Rivera, R. J. Cava, and C. L. Broholm, *Phys. Rev. B* **93**, 014433 (2016).
- ¹⁸⁶ F. Seitz and D. Turnbull, *Solid State Physics*, Solid State Physics No. v. 9 (Elsevier Science, 1959).
- ¹⁸⁷ H. T. Hutchings, *Solid State Phys.* **16**, 227 (1964).
- ¹⁸⁸ Y.-J. Kim, A. P. Sorini, C. Stock, T. G. Perring, J. van den Brink, and T. P. Devereaux, *Phys. Rev. B* **84**, 085132 (2011).